

Entropy-based viscous regularization for the multi-dimensional Euler equations in low-Mach and transonic flows

Marc O. Delchini^a, Jean C. Ragusa^{*,a}, Ray A. Berry^b

^a*Department of Nuclear Engineering, Texas A&M University, College Station, TX 77843, USA*

^b*Idaho National Laboratory, Idaho Falls, ID 83415, USA*

Abstract

The entropy viscosity method, introduced by Guermond et al. [1, 2], is extended to the multi-dimensional Euler equations for both subsonic (very low Mach numbers) and supersonic flows. We show that the current definition of the viscosity coefficients [1, 2] is not adapted to low-Mach flows and we provide a robust alternate definition valid for any Mach number value. The new definitions are derived from a low-Mach asymptotic study. In addition, the entropy minimum principle is used to derive the viscous regularization terms for Euler equations with variable area for nozzle flow problems. Various 1-D and 2-D numerical tests are presented : flow in a converging-diverging nozzle, Leblanc shock tube, slow moving shock, strong shock for liquid phase, subsonic flow around a 2-D cylinder and over a circular hump, and supersonic flow in a compression corner. Convergence studies are performed using analytical solutions in 1-D. The ideal gas and stiffened gas equations of state are employed.

Key words: entropy viscosity method, viscous stabilization method, low-Mach regime, shocks, Euler equations with variable area .

1. Introduction

Over the past years an increasing interest has been raised for computational methods that can solve both compressible and incompressible flows. In engineering applications, there is often the need to solve for complex flows where a near incompressible regime or low Mach flow coexists with a supersonic flow domain. For example, such flows are encountered in aerodynamics in the study of airships. In the nuclear industry, flows are nearly in the incompressible regime but compressible effects cannot be neglected because of the heat source and thus

*Corresponding author

Email addresses: `delchmo@tamu.edu` (Marc O. Delchini), `jean.ragusa@tamu.edu` (Jean C. Ragusa), `ray.berry@inl.gov` (Ray A. Berry)

9 needs to be accurately resolved.
 10 When solving the multi-D Euler equations for a wide range of Mach numbers,
 11 multiple problems must be addressed: stability, accuracy and acceleration of
 12 the convergence in the low Mach regime. Because of the hyperbolic nature of
 13 the equations, shocks can form during transonic and supersonic flows, and re-
 14 quire the use of the numerical methods in order to stabilize the scheme and
 15 correctly resolve the discontinuities. The literature offers a wide range of sta-
 16 bilization methods: flux-limiter [3, 4], pressure-based viscosity method ([5]),
 17 Lapidus method ([6, 7, 8]), and the entropy-viscosity method([1, 2]) among oth-
 18 ers. These numerical methods are usually developed using simple equations of
 19 state and tested for transonic and supersonic flows where the disparity between
 20 the acoustic waves and the fluid speed is not large since the Mach number is
 21 of order one. This approach, however, leads to a well-known accuracy problem
 22 in the low Mach regime where the fluid velocity is smaller than the speed of
 23 sound by multiple order of magnitude. The numerical dissipative terms become
 24 ill-scaled in the low Mach regime and lead to the wrong numerical solution by
 25 changing the nature of the equations solved. This behavior is well documented
 26 in the literature [9, 10, 11] and often treated by performing a low Mach asymp-
 27 totic study of the multi-D Euler equation. This method was originally used [9]
 28 to show convergence of the compressible multi-D Euler equations to the incom-
 29 pressible ones. Thus, by using the same method, the effect of the dissipative
 30 terms in the low Mach regime, can be understood and, when needed, a fix is
 31 developed in order to ensure the convergence of the equations to the correct
 32 physical solution. This approach was used as a "fixing" method for multiple
 33 well known stabilization methods alike Roe scheme ([12]) and SUPG [11] while
 34 preserving the original stabilization properties of shocks. Furthermore, it is also
 35 of common knowledge that low-Mach steady-state solutions can be difficult to
 36 obtain with a temporal explicit solver. For stability purpose, the time step must
 37 be chosen inversely proportional to the largest eigenvalue of the system which is
 38 approximately the speed of sound, c , for slow flows. However, other waves are
 39 convected at the fluid speed, which is much slower. Hence, these waves do not
 40 change very much over a time step. Thus, thousands of time steps are required
 41 to reach a steady state. Acceleration techniques were developed and proved
 42 efficient [10], but require to modify the temporal derivatives of the equation
 43 and thus, can only be used for steady-state flows. To avoid to modifying the
 44 temporal derivatives, the temporal implicit capabilities of the MOOSE multi-
 45 physics framework [13] is used. Such a choice should allow us to quickly obtain
 46 low-Mach steady-state solutions, while preserving the accuracy of the transient
 47 solution, but also requires a preconditioner.
 48 We propose, through this paper, to investigate how the entropy viscosity method,
 49 when applied to the multi-D Euler equations with variable area, behaves in the
 50 low Mach regime. This method was initially introduced by Guermond et al.
 51 to solve for the hyperbolic systems and has shown good results when used for
 52 solving the multi-D Euler equations for supersonic flows with various discretiza-
 53 tion schemes. More importantly, it is simple to implement, can be used with
 54 unstructured grids, and its dissipative terms are consistent with the entropy

55 minimum principle and it has proven valid for any equation of state under cer-
 56 tain conditions [14].

57
 58 This paper is organized as follows: in Section 2 the current definition of
 59 the entropy viscosity method is recalled, and inconsistency with the low Mach
 60 regime are pointed out. Since our interest is in the variable area version of the
 61 multi-D Euler equation, the reader is guided through the steps leading to the
 62 derivation of the dissipative terms on the model of [14]. Then in Section 3, a
 63 new definition of the viscosity coefficient is introduced and derived from a low
 64 Mach asymptotic study. After detailing the spatial and temporal discretization
 65 method in Section 5, 1-D and 2-D numerical results are presented in Section 6
 66 for a wide range of Mach numbers: low Mach flow over a cylinder and a circular
 67 bump, and supersonic flow in a compression corner [15]. Convergence studies
 68 are performed in 1-D, in order to demonstrate the accuracy of the solution.
 69

70 2. The Entropy Viscosity Method

71 2.1. Background

72 The Euler equations are given by

$$\partial_t \rho + \vec{\nabla} \cdot (\rho \vec{u}) = 0 \quad (1a)$$

$$\partial_t (\rho \vec{u}) + \vec{\nabla} \cdot (\rho \vec{u} \otimes \vec{u} + P \mathbb{I}) = 0 \quad (1b)$$

$$\partial_t (\rho E) + \vec{\nabla} \cdot [\vec{u} (\rho E + P)] = 0 \quad (1c)$$

75 where ρ , $\rho \vec{u}$ and ρE are the density, the momentum and the total energy, re-
 76 spectively, and will be referred to as the conservative variables. \vec{u} is the fluid
 77 velocity and its specific internal energy is denoted by $e = E - \frac{u^2}{2}$. An equation
 78 of state, dependent upon ρ and e , is used to compute the pressure P . The tensor
 79 product $\vec{a} \otimes \vec{b}$ is such that $(\vec{a} \otimes \vec{b})_{i,j} = a_i b_j$. The identity tensor is denoted by \mathbb{I} .

80 Next, the entropy viscosity method [1, 2, 16, 17] applied to Eq. (1) is recalled.
 81 The method consists of adding dissipative terms with a viscosity coefficient mod-
 82 ulated by the entropy production; this allows for a high-order accuracy when
 83 the solution is smooth (provided that the spatial and temporal discretizations
 84 also are high order). The derivation of the viscous regularization (or dissipa-
 85 tive terms) is carried out to be consistent with the entropy minimum principle;
 86 details and proofs of the derivation can be found in [14]. The viscous regular-
 87 ization thus obtained is valid for any equation of state as long as the physical
 88 entropy function s which is concave (or $-s$ is a convex function) with respect
 89 to the internal energy e and the specific volume $1/\rho$. The Euler equations with
 90 viscous regularization become

$$\partial_t \rho + \vec{\nabla} \cdot (\rho \vec{u}) = \vec{\nabla} \cdot (\kappa \vec{\nabla} \rho) \quad (2a)$$

$$\partial_t (\rho \vec{u}) + \vec{\nabla} \cdot (\rho \vec{u} \otimes \vec{u} + P \mathbf{I}) = \vec{\nabla} \cdot (\mu \rho \vec{\nabla}^s \vec{u} + \kappa \vec{u} \otimes \vec{\nabla} \rho) \quad (2b)$$

$$\partial_t (\rho E) + \vec{\nabla} \cdot [\vec{u} (\rho E + P)] = \vec{\nabla} \cdot \left(\kappa \vec{\nabla} (\rho e) + \frac{1}{2} \|\vec{u}\|^2 \kappa \vec{\nabla} \rho + \rho \mu \vec{u} \vec{\nabla} \vec{u} \right) \quad (2c)$$

where κ and μ are positive viscosity coefficients. $\vec{\nabla}^s \vec{u}$ denotes the symmetric gradient operator that guarantees the method to be rotationally invariant [14]. The viscosity coefficients are key ingredients in the viscous regularization of Eq. (2). Other stabilization approaches have been proposed in the literature, for instance, the Lapidus method [8, 6] or pressure-based viscosity methods [5]. Here, we follow the work of Guermond et al. and define the viscosity coefficients, κ and μ , based on the local entropy production. These coefficients are numerically evaluated using the local entropy residual $R_e(\vec{r}, t)$ defined in Eq. (3); $R_e(\vec{r}, t)$ is known to be peaked in shocks and vanishingly small elsewhere [18].

$$R_e(\vec{r}, t) := \partial_t s + \vec{u} \cdot \vec{\nabla} s \quad (3)$$

In the current version of the method, the ratio of κ to μ is defined through a numerical Prandtl number, $\text{Pr} = \kappa/\mu$. Pr is a user-defined parameter and is usually taken in the range $[0.001; 1]$. Since the entropy residual $R_e(\vec{r}, t)$ may be extremely large in shocks, the definition of the viscosity coefficients also includes a first-order viscosity coefficient that serves as an upper bound for the entropy-based viscosity coefficients. The first-order viscosity coefficients, denoted by μ_{\max} and κ_{\max} , are chosen so that the numerical scheme becomes equivalent to an upwind scheme when the first-order coefficients are employed. The upwind scheme is known to be over-dissipative but guarantees monotonicity [18]. In practice, the viscosity coefficients only saturate to the first-order viscosity coefficients in shocks and are much smaller elsewhere, hence avoiding the over-dissipation of the upwind method. The first-order viscosity coefficients μ_{\max} and κ_{\max} are equal and set proportional to the largest local eigenvalue $\|\vec{u}\| + c$:

$$\mu_{\max}(\vec{r}, t) = \kappa_{\max}(\vec{r}, t) = \frac{h}{2} (\|\vec{u}(t, \vec{r})\| + c(t, \vec{r})), \quad (4)$$

where h denotes the local grid size (for higher than linear finite element representations, h is defined as the ratio of the grid size to the polynomial order of the test functions used, see Eq. 2.4 in [17]). For simplicity, the first-order viscosity coefficient will only be referred to as the $\kappa_{\max}(\vec{r}, t)$. In practice, these quantities are evaluated within a given cell K at quadrature points:

$$\kappa_{\max}^K(\vec{r}_q, t) = \frac{h_K}{2} (\|\vec{u}(t, \vec{r}_q)\| + c(t, \vec{r}_q)), \quad (5)$$

where \vec{r}_q denotes the position of a quadrature point. As stated earlier, the entropy viscosity coefficients, which we denote by κ_e and μ_e , are set proportional to the entropy production evaluated by computing the local entropy residual R_e . The definitions also include the inter-element jump $J[s]$ of the entropy flux, allowing for the detection of discontinuities other than shocks (e.g., contact).

$$\mu_e^K(\vec{r}_q, t) = h_K^2 \frac{\max(|R_e^K(\vec{r}_q, t)|, J^K[s](t))}{\|s - \bar{s}\|_\infty} \quad (6a)$$

126

$$\kappa_e^K(\vec{r}_q, t) = Pr \mu_e^K(\vec{r}_q, t) \quad (6b)$$

127 where $\|\cdot\|_\infty$ and $\bar{\cdot}$ denote the L_∞ -norm and the average operator over the
 128 entire computational domain, respectively. The definition of the entropy jump
 129 $J[s]$ is spatial discretization-dependent and examples of definitions can be found
 130 in [17] for discontinuous Galerkin discretization. For continuous finite element
 131 methods (FEM), the jump of a given quantity is defined as the change of its
 132 normal derivative ($\partial_n = \vec{\nabla} \cdot \vec{n}$) across the common face separating the two
 133 elements, and will be further referred to as the inter-element jump. We take the
 134 largest value over all faces f present on the boundary ∂K of element K :

$$J^K[s](t) = \max_{f \in \partial K} \max_{\vec{r}_q \in f} [\vec{\nabla} s(\vec{r}_q, t) \cdot \vec{n}(\vec{r}_q)]_f, \quad (7)$$

135 where $\llbracket a(\vec{r}_q) \rrbracket_f$ denotes the inter-element jump in $a(\vec{r})$ at quadrature point \vec{r}_q
 136 on face f (the quadrature points \vec{r}_q are taken on the faces f of the element K).
 137 With the definition given in Eq. (7), the jump is constant over each element K
 138 of the computational domain. The denominator $\|s - \bar{s}\|_\infty$ is used for dimen-
 139 sionality purposes. Currently, there is no theoretical justification for choosing
 140 the denominator beyond a dimensionality argument. Finally, the viscosity co-
 141 efficients μ and κ are as follows:

$$\mu(\vec{r}, t) = \min(\mu_e(\vec{r}, t), \mu_{\max}(\vec{r}, t)) \quad \text{and} \quad \kappa(\vec{r}, t) = \min(\kappa_e(\vec{r}, t), \kappa_{\max}(\vec{r}, t)). \quad (8)$$

142 Given these definitions, we have the following properties. In shock regions, the
 143 entropy viscosity coefficients will experience a peak because of entropy produc-
 144 tion and thus will saturate to the first-order viscosity. The first-order coefficients
 145 are known to be over-dissipative and will smooth out any oscillatory behavior.
 146 Elsewhere in the domain, entropy production will be small and the viscosity
 147 coefficients μ and κ will remain small. High-order accuracy for entropy-based
 148 viscous stabilization has demonstrated using several 1-D shock tube examples
 149 and various 2-D tests [1, 2, 17].

150 2.2. Issues in the Low-Mach Regime

151 In the low-Mach Regime, the flow is known to approach isentropic, resulting
 152 in very little entropy production. Since the entropy viscosity method is directly
 153 based on the evaluation of the local entropy production, it is of interest to
 154 study how the entropy viscosity coefficients μ_e and κ_e scale in the low-Mach
 155 regime. In practice, the entropy residual R_e will be very small in that regime
 156 and so will be the denominator $\|s - \bar{s}\|_\infty$, thus making the definition of the
 157 viscosity coefficients in Eq. (6) undetermined and likely ill-scaled. One possible
 158 approach would consist of expanding the numerator and denominator in terms
 159 of the Mach number and deriving its limit when the Mach number goes to zero.
 160 Such derivation may not be straightforward, especially for general equations of
 161 state. However, this can be avoided by noting that the entropy residual R_e
 162 can be recast as a function of pressure, density, velocity, and speed of sound as

shown in Eq. (9) of Section 3.1. This alternate entropy residual definition is the basis for the low-Mach analysis carried out in this paper and possesses several advantages that are detailed next.

3. An All-speed Reformulation of the Entropy Viscosity Method

In this section, the entropy residual R_e is recast as a function of pressure, density, velocity and speed of sound. Then, a low-Mach asymptotic study is carried out for the Euler equations with viscous regularization in order to derive an appropriate normalization parameter that is valid in the low-Mach regime as well as for transonic and supersonic flows.

3.1. New Definition of the Entropy Production Residual

The first step in defining viscosity coefficients that behave well in the low-Mach limit is to recast the entropy residual in terms of thermodynamic variables. This provides physical insight on possible normalization choices that can be valid in both low-Mach and transonic flows. The alternate definition of the entropy residual, the derivation of which is given in Appendix A, is given

$$R_e(\vec{r}, t) := \partial_t s + \vec{u} \cdot \vec{\nabla} s = \frac{Ds}{Dt} = \frac{s_e}{P_e} \left(\underbrace{\frac{DP}{Dt} - c^2 \frac{D\rho}{Dt}}_{\widetilde{R}_e(\vec{r}, t)} \right), \quad (9)$$

where $\frac{D}{Dt}$ denotes the material derivative ($\frac{D}{Dt} := \frac{\partial}{\partial t} + \vec{u} \cdot \vec{\nabla}$), and x_y is the standard shorthand notation for the partial derivative of x with respect to y , e.g., $P_e := \frac{\partial P}{\partial e}$. The entropy residuals R_e and \widetilde{R}_e are proportional to one another and will experience similar variations in space and time. Thus, one may elect to employ \widetilde{R}_e instead of R_e for the evaluation of the local entropy residual. The new expression presents several advantages:

- An analytical expression of the entropy function s is no longer needed: the residual \widetilde{R}_e is evaluated using the local values of pressure, density, velocity and speed of sound. Deriving an entropy function for some complex equation of states may be difficult;
- Suitable normalizations for the residual \widetilde{R}_e can be devised. Examples include the pressure itself or combinations of the density, the speed of sound and the norm of the velocity, i.e., ρc^2 , $\rho c ||\vec{u}||$ or $\rho ||\vec{u}||^2$.

Denoting the normalization of \widetilde{R}_e by norm_P , the entropy-based viscosity coefficients μ_e and κ_e can be re-defined as follows:

$$\mu_e^K(\vec{r}, t) = h_K^2 \frac{\max \left(|\widetilde{R}_e^K(\vec{r}_q, t)|, ||\vec{u}(\vec{r}_q, t)|| J^K[P](t), ||\vec{u}(\vec{r}_q, t)|| c^2(\vec{r}_q, t) ||J^K[\rho](t)|| \right)}{\text{norm}_P^\mu}, \quad (10a)$$

193 and

$$\kappa_e^K(\vec{r}, t) = h_K^2 \frac{\max \left(|\widetilde{R}_e^K(\vec{r}_q, t)|, \|\vec{u}(\vec{r}_q, t)\| J^K[P](t), \|\vec{u}(\vec{r}_q, t) c^2(\vec{r}_q, t)\| J^K[\rho](t) \right)}{\text{norm}_P^\kappa}. \quad (10b)$$

194 Note that now the jump operator acts on the variables appearing in \widetilde{R}_e , namely,
 195 pressure and density. The μ and κ coefficients are kinematic viscosities (units
 196 of m^2/s); the normalization parameters norm_P are thus in units of pressure,
 197 hence the use of the subscript P . Note also that we are not requiring the same
 198 normalization for both μ_e and κ_e so the entropy viscosity coefficients can be
 199 different. The low-Mach asymptotic study presented next will determine the
 200 proper normalization.

201 3.2. Asymptotic Study in the Low-Mach Regime

202 The Euler equations with viscous stabilization, Eq. (6), bear some simi-
 203 larities with the Navier-Stokes equations in the sense that dissipative terms
 204 (containing second-order spatial derivatives) are present in both sets of equa-
 205 tions. An abundant literature exists regarding the low-Mach asymptotics of the
 206 Navier-Stokes equations [9, 10, 11, 19]. The asymptotic study presented here is
 207 inspired by the work of Muller et al. [19] where an asymptotic derivation for
 208 the Navier-Stokes was presented. We remind the reader that the objective is to
 209 determine appropriate scaling for the entropy viscosity coefficients so that the
 210 dissipative terms remain well-scaled for two limit cases: (i) the isentropic limit
 211 where Euler equations degenerate to an incompressible system of equations in
 212 the low-Mach limit and (ii) the non-isentropic limit with formation of shocks.
 213 The isentropic limit of the Euler equations with viscous regularization should
 214 yield incompressible fluid flow solutions in the low-Mach limit, namely, that
 215 the pressure fluctuations are of the order M^2 and that the velocity satisfies the
 216 divergence constraint $\vec{\nabla} \cdot \vec{u}_0 = 0$ [9, 10, 11]. For non-isentropic situations, shocks
 217 may form for any value of Mach number and the minimum entropy principle
 218 should still be satisfied so that numerical oscillations, if any, be controlled by the
 219 entropy viscosity method independently of the value of the Mach number. Our
 220 objective is to determine the appropriate scaling for the Reynolds and Péclet
 221 numbers, Re_∞ and Pé_∞ , in these two limit cases.

In this Section, we are interested in the isentropic limit; the non-isentropic
 case is treated later. The first step in the study of the limit cases (i) and (ii)
 is to re-write Eq. (2) in a non-dimensional manner. To do so, the following
 variables are introduced:

$$\rho^* = \frac{\rho}{\rho_\infty}, \quad u^* = \frac{u}{u_\infty}, \quad P^* = \frac{P}{\rho_\infty c_\infty^2}, \quad E^* = \frac{E}{c_\infty^2},$$

$$x^* = \frac{x}{L_\infty}, \quad t^* = \frac{t}{L_\infty/u_\infty}, \quad \mu^* = \frac{\mu}{\mu_\infty}, \quad \kappa^* = \frac{\kappa}{\kappa_\infty}, \quad (11)$$

222 where the subscript ∞ denote the far-field or stagnation quantities and the
 223 superscript $*$ stands for the non-dimensional variables. The far-field reference

quantities are chosen such that the dimensionless flow quantities are of order 1.
The reference Mach number is given by

$$M_\infty = \frac{u_\infty}{c_\infty}, \quad (12)$$

where c_∞ is a reference value for the speed of sound. Then, the scaled Euler equations with viscous regularization are:

$$\partial_{t^*} \rho^* + \vec{\nabla}^* \cdot (\rho^* \vec{u}^*) = \frac{1}{\text{Pé}_\infty} \vec{\nabla}^* \cdot (\kappa^* \vec{\nabla}^* \rho^*) \quad (13a)$$

$$\begin{aligned} \partial_{t^*} (\rho^* \vec{u}^*) + \vec{\nabla}^* \cdot (\rho^* \vec{u}^* \otimes \vec{u}^*) + \frac{1}{M_\infty^2} \vec{\nabla}^* P^* &= \frac{1}{\text{Re}_\infty} \vec{\nabla}^* \cdot (\rho^* \mu^* \vec{\nabla}^{s,*} \vec{u}^*) \\ &+ \frac{1}{\text{Pé}_\infty} \vec{\nabla}^* \cdot (\vec{u}^* \otimes \kappa^* \vec{\nabla}^* \rho^*) \end{aligned} \quad (13b)$$

$$\begin{aligned} \partial_{t^*} (\rho^* E^*) + \vec{\nabla}^* \cdot [\vec{u}^* (\rho^* E^* + P^*)] &= \frac{1}{\text{Pé}_\infty} \vec{\nabla}^* \cdot (\kappa^* \vec{\nabla}^* (\rho^* e^*)) \\ &+ \frac{M_\infty^2}{\text{Re}_\infty} \vec{\nabla}^* \cdot (\vec{u}^* \rho^* \mu^* \vec{\nabla}^{s,*} \vec{u}^*) + \frac{M_\infty^2}{2\text{Pé}_\infty} \vec{\nabla}^* \cdot (\kappa^* (u^*)^2 \vec{\nabla}^* \rho^*) , \end{aligned} \quad (13c)$$

where the numerical Reynolds (Re_∞) and Péclet (Pé_∞) numbers are defined as:

$$\text{Re}_\infty = \frac{u_\infty L_\infty}{\mu_\infty} \text{ and } \text{Pé}_\infty = \frac{u_\infty L_\infty}{\kappa_\infty} . \quad (14)$$

Note that the Prandtl number used in the original version of the entropy viscosity method is simply given by

$$\text{Pr}_\infty = \text{Pé}_\infty / \text{Re}_\infty . \quad (15)$$

For simplicity, we use here the ideal gas equation of state; its non-dimensionalized expression is given by

$$P^* = (\gamma - 1) \rho^* \left(E^* - \frac{1}{2} M_\infty^2 (u^*)^2 \right) = (\gamma - 1) \rho^* e^* . \quad (16)$$

The numerical Reynolds and Péclet numbers defined in Eq. (14) are related to the entropy viscosity coefficients μ_∞ and κ_∞ . Thus, once a scaling (in powers of M_∞) is obtained for Re_∞ and Pé_∞ , the corresponding normalization parameters norm_P^μ and norm_P^κ will automatically be set. For brevity, the superscripts $*$ are omitted in the remainder of this section.

In the low-Mach isentropic limit, shocks cannot form and the compressible Euler equations are known to converge to the incompressible equations when the Mach number tends to zero. When adding dissipative terms, as is the case with the entropy viscosity method, the main properties of the low-Mach asymptotic

limit must be preserved. We begin by expanding each variable in powers of the Mach number. As an example, the expansion for the pressure is given by:

$$P(\vec{r}, t) = P_0(\vec{r}, t) + P_1(\vec{r}, t)M_\infty + P_2(\vec{r}, t)M_\infty^2 + \dots \quad (17)$$

By studying the resulting momentum equations for various powers of M_∞ , it is observed that the leading order and first-order pressure terms, P_0 and P_1 , are spatially constant if and only if $\text{Re}_\infty = \text{Pé}_\infty = 1$. In this case, at order M_∞^{-2} :

$$\vec{\nabla} P_0 = 0 \quad (18a)$$

and, at order M_∞^{-1} ,

$$\vec{\nabla} P_1 = 0. \quad (18b)$$

Using the scaling $\text{Re}_\infty = \text{Pé}_\infty = 1$, the leading-order (order 1) expressions for the continuity, momentum, and energy equations are:

$$\partial_t \rho_0 + \vec{\nabla} \cdot (\rho \vec{u})_0 = \vec{\nabla} \cdot (\kappa \vec{\nabla} \rho)_0 \quad (19a)$$

$$\partial_t (\rho \vec{u})_0 + \vec{\nabla} \cdot (\rho \vec{u} \otimes \vec{u})_0 + \vec{\nabla} P_2 = \vec{\nabla} \cdot (\rho \mu \vec{\nabla}^s \vec{u} + \kappa \vec{u} \otimes \vec{\nabla} \rho)_0 \quad (19b)$$

$$\partial_t (\rho E)_0 + \vec{\nabla} \cdot [\vec{u}(\rho E + P)]_0 = \vec{\nabla} \cdot (\kappa \vec{\nabla}(\rho e))_0 \quad (19c)$$

where the notation $(fg)_0$ means that we only keep the 0th order terms in the product fg . The leading-order of the equation of state is given by

$$P_0 = (\gamma - 1)(\rho E)_0. \quad (20)$$

Using Eq. (20), the energy equation can be recast as a function of the leading-order pressure, P_0 , as follows:

$$\partial_t P_0 + \gamma \vec{\nabla} \cdot (\vec{u} P)_0 = \vec{\nabla} \cdot (\kappa \vec{\nabla}(P))_0 \quad (21)$$

From Eq. (18a), we infer that P_0 is spatially constant. Thus, Eq. (21) becomes

$$\frac{1}{\gamma P_0} \frac{dP_0}{dt} = -\vec{\nabla} \cdot \vec{u}_0 \quad (22)$$

and, at steady state, we have

$$\vec{\nabla} \cdot \vec{u}_0 = 0. \quad (23)$$

That is, the leading-order of velocity is divergence-free. The same reasoning can be applied to the leading-order of the continuity equation (Eq. (19a)) to show that the material derivative of the density is zero:

$$\frac{D\rho_0}{Dt} := \partial_t \rho_0 + \vec{u}_0 \cdot \vec{\nabla} \rho_0 = 0. \quad (24)$$

Therefore, we conclude that by setting the Reynolds and Péclet numbers to one, the incompressible fluid results are retrieved in the low-Mach limit when employing the compressible Euler equations with viscous regularization terms present. In addition, the scaling of the Prandtl number can also be obtained using Eq. (15), hence clarifying the use of the numerical Prandtl in the original entropy viscosity method [1].

267 3.3. Scaling of Re_∞ and $Pé_\infty$ for non-isentropic flows

268 Next, we consider the non-isentropic case. Recall that even subsonic flows
 269 can present shocks (for instance, a step initial condition in the pressure will trig-
 270 ger shock formation, independently of the Mach number). The non-dimensional
 271 form of the Euler equations given in Eq. (13) provides some insight on the dom-
 272 inant terms as a function of the Mach number. This is particular obvious in
 273 the momentum equation, Eq. (13b), where the gradient of pressure is scaled
 274 by $1/M_\infty^2$. In the non-isentropic case, we no longer have $\frac{\vec{\nabla} P}{M_2} = \vec{\nabla} P_2$ and this
 275 pressure gradient term may need to be stabilized by some dissipative terms of
 276 the same scaling so as to prevent spurious oscillations from forming. This leads
 277 to the following three possible requirements regarding the non-dimensionalized
 278 Reynolds and Péclet numbers for non-isentropic flows: (a) $Re_\infty = M_\infty^2$ and
 279 $Pé_\infty = 1$, (b) $Re_\infty = 1$ and $Pé_\infty = M_\infty^2$, or (c) $Re_\infty = Pé_\infty = M_\infty^2$. Any of
 280 these choices will also affect the stabilization of the continuity and energy equa-
 281 tions. For instance, using a Péclet number equal to M_∞^2 may effectively stabilize
 282 the continuity equation in the shock region but this may also add an excessive
 283 amount of dissipation for subsonic flows at the location of the contact wave.
 284 Such a behavior may not be suitable for accuracy purpose, making options (b)
 285 and (c) inappropriate. The same reasoning, left to the reader, can be carried
 286 out for the energy equation (Eq. (13c)) and results in the same conclusion. The
 287 remaining choice, option (a), has the proper scaling: in this case, only the dis-
 288 sipation terms involving $\vec{\nabla}^{s,*} \vec{u}^*$ scale as $1/M_\infty^2$ since $Re_\infty = M_\infty^2$, leaving the
 289 regularization of the continuity equation unaffected because $Pé_\infty = 1$.

290 3.4. New normalization for the entropy residual

291 The study of the above limit cases yields two different possible scalings for
 292 the Reynolds number: $Re_\infty = 1$ in the isentropic case and $Re_\infty = M_\infty^2$ for
 293 non-isentropic case, whereas the numerical Péclet number always scales as one.
 294 In order to have a stabilization method valid for a wide range of Mach numbers,
 295 including situations with shocks, these two scalings should be combined in a
 296 unique definition. The non-dimensionalized entropy residual, \widetilde{R}_e^* , scales differ-
 297 ently for differing flow types (isentropic and non-isentropic) [20]. For isentropic
 298 flows, the non-dimensionalized entropy residual is known to scale as the Mach
 299 number. For non-isentropic flows, the non-dimensionalized entropy residual is
 300 large and presents a peak at the location of the shock. Thus, by inspecting
 301 the *local* variation of the non-dimensionalized entropy residual, an appropriate
 302 transition for the scaling of the Reynolds number can be obtained:

$$Re_\infty = \begin{cases} M^2 & \text{if } \left| \widetilde{R}_e^* \right| \geq M \text{ (i.e., non-isentropic flow)} \\ 1 & \text{otherwise} \end{cases} \quad (25)$$

303 Now that we have determined a scaling for Re_∞ and Re_∞ , the normalization
 304 parameters norm_P^μ and norm_P^κ can be finalized. For brevity, only the steps
 305 leading to the derivation of norm_P^κ are provided; the algebra for norm_P^μ is similar.

Using the definition of the viscosity coefficients given in Eq. (10) and the scaling of Eq. (11), it can be shown that:

$$\kappa_\infty = \frac{\rho_\infty c_\infty^2 u_\infty L}{\text{norm}_{P,\infty}^\kappa}, \quad (26)$$

where $\text{norm}_{P,\infty}$ is the reference far-field quantity for the normalization parameter norm_P . Substituting Eq. (26) into Eq. (14) and recalling that the numerical Péclet number scales as unity, we obtain:

$$\text{norm}_{P,\infty}^\kappa = \text{Pé}_\infty \rho_\infty c_\infty^2 = \rho_\infty c_\infty^2. \quad (27)$$

Eq. (27) provides a proper normalization factor to define the κ viscosity coefficient. Similarly, the normalization parameter norm_P^μ for the μ viscosity coefficient is derived for the two cases given in Eq. (25):

$$\text{norm}_P^\mu = \text{Re}_\infty \rho_\infty c_\infty^2 = \begin{cases} \rho \|\vec{u}\|^2 & \text{if } |\widetilde{R_e^*}| \geq M \text{ (i.e., non-isentropic flow)} \\ \rho c^2 = \text{norm}_P^\kappa & \text{otherwise} \end{cases}. \quad (28)$$

Finally, we summarize the definition of the viscosity coefficients μ and κ devised here:

$$\mu(\vec{r}, t) = \min(\mu_{\max}(\vec{r}, t), \mu_e(\vec{r}, t)) \text{ and } \kappa(\vec{r}, t) = \min(\mu_{\max}(\vec{r}, t), \kappa_e(\vec{r}, t)) \quad (29a)$$

where the first-order viscosity is given by

$$\kappa_{\max}(\vec{r}, t) = \mu_{\max}(\vec{r}, t) = \frac{h}{2} (\|\vec{u}\| + c) \quad (29b)$$

and the entropy viscosity coefficients by

$$\kappa_e(\vec{r}, t) = \frac{h^2 \max(\widetilde{R_e}, J)}{\rho c^2} \text{ and } \mu_e(\vec{r}, t) = \frac{h^2 \max(\widetilde{R_e}, J)}{\text{norm}_P^\mu} \quad (29c)$$

with the jumps given by

$$J = \|\vec{u}\| \max([\vec{\nabla} P \cdot \vec{n}], c^2 [\vec{\nabla} \rho \cdot \vec{n}]) \quad (29d)$$

where norm_P^κ is computed from Eq. (28). The jump J is a function of the jump of pressure and density gradients across the face with respect to its normal vector \vec{n} . Then, the largest value over all faces is determined and used in the definition of the viscosity coefficients.

With the definition of the viscosity coefficients μ and κ proposed in Eq. (29), the low-Mach asymptotic limit is ensured for isentropic flow, and transonic flows with shocks will be correctly resolved. As the flow becomes locally supersonic, the viscosity coefficients μ and κ will be of the same order of magnitude, which is consistent with the original definition of the entropy viscosity method [1, 2] recalled in Section 2.1.

329 4. Extension of the entropy viscosity technique Euler equations with 330 variable area

331 Fluid flows in nozzles and in pipes of varying cross-sectional area can be
332 modeled using the variable-area variant of the Euler equations, where the con-
333 servative variables are now multiplied by the area A . In addition, these equa-
334 tions differ from the standard Euler equations in that the momentum equation
335 Eq. (30b) contains a non-conservative term proportional to the area gradient.
336 For the purpose of this paper, the variable area is assumed to be a smooth
337 function of space only.

$$\partial_t (\rho A) + \vec{\nabla} \cdot (\rho \vec{u} A) = 0 \quad (30a)$$

$$\partial_t (\rho \vec{u} A) + \vec{\nabla} \cdot [A (\rho \vec{u} \otimes \vec{u} + P \mathbb{I})] = P \vec{\nabla} A \quad (30b)$$

$$\partial_t (\rho E A) + \vec{\nabla} \cdot [\vec{u} A (\rho E + P)] = 0 \quad (30c)$$

340 The application of the entropy viscosity method to the Euler equations with
341 variable area is not fundamentally different to its application to the standard
342 Euler equations. However, we need to derive the associated dissipative terms
343 and verify that the entropy minimum principle is still satisfied. The variable-
344 area Euler equations with viscous regularization are given below; details of the
345 derivation are provided in Appendix B.

$$\partial_t (\rho A) + \vec{\nabla} \cdot (\rho \vec{u} A) = \vec{\nabla} \cdot (A \kappa \vec{\nabla} \rho) \quad (31a)$$

$$\partial_t (\rho \vec{u} A) + \vec{\nabla} \cdot [A (\rho \vec{u} \otimes \vec{u} + P \mathbb{I})] = P \vec{\nabla} A + \vec{\nabla} \cdot \left[A \left(\mu \rho \vec{\nabla}^s \vec{u} + \kappa \vec{u} \otimes \vec{\nabla} \rho \right) \right] \quad (31b)$$

$$\partial_t (\rho A E) + \vec{\nabla} \cdot [\vec{u} A (\rho E + P)] = \vec{\nabla} \cdot \left[A \left(\kappa \vec{\nabla} (\rho e) + \frac{1}{2} \|\vec{u}\|^2 \kappa \vec{\nabla} \rho + \rho \mu \vec{u} \vec{\nabla}^s \vec{u} \right) \right] \quad (31c)$$

348 The dissipative terms are quite similar to the ones obtained for the standard
349 Euler equations: each dissipative flux is simply multiplied by the variable area
350 A in order to ensure conservation of the dissipative flux. When assuming a
351 constant area, Eq. (2) are recovered.

352 A low-Mach asymptotic limit of the multi-D Euler equations with variable
353 area on the same model as in Section 3.2 will lead to the divergence constraint
354 $\vec{\nabla} \cdot (\vec{u} A) = 0$ that can be recast as $\vec{\nabla} \cdot \vec{u} = -\vec{u} \cdot \vec{\nabla} A / A$. The gradient of the
355 area acts as a source term and will force the fluid to accelerate or decelerate,
356 depending on its sign.

357 5. Discretizations and Solution Techniques

358 In this section, we briefly describe the spatial and temporal techniques used
359 to discretize and solve the system of equations Eq. (31). For conciseness, we
360 re-write the system of equations in the following form:

$$\partial_t \mathbf{U} + \vec{\nabla} \cdot \vec{\mathbf{F}}(\mathbf{U}) = \mathbf{S} + \vec{\nabla} \cdot \mathbf{D}(\mathbf{U}) \vec{\nabla} \mathbf{U} \quad (32)$$

where $\mathbf{U} = [\rho A, \rho \vec{u} A, \rho E A]^T$ is the solution vector, \mathbf{F} denotes the inviscid flux

$$\vec{\mathbf{F}} \equiv \begin{bmatrix} \rho u A \\ (\rho u^2 + p) A \\ u(\rho E + P) A \end{bmatrix} \quad (33)$$

and \mathbf{S} is a source term that contains the non-conservative term $P \vec{\nabla} A$. The term $\vec{\nabla} \cdot D(\mathbf{U}) \vec{\nabla} \mathbf{U}$ stands for the artificial dissipative terms.

5.1. Spatial and Temporal Discretizations

The system of equations given in Eq. (32) is discretized using a continuous Galerkin finite element method and temporal integrators available through the MOOSE multiphysics framework [13].

5.1.1. Continuous Finite Elements

In order to apply the continuous finite element method, Eq. (32) is multiplied by a test function $\mathbf{W}(\vec{r})$, integrated by parts and each integral is decomposed into a sum of integrals over each element K of the discrete mesh Ω . The following weak form is obtained:

$$\begin{aligned} \sum_K \int_K \partial_t \mathbf{U} \mathbf{W} - \sum_K \int_K \vec{\mathbf{F}}(\mathbf{U}) \cdot \vec{\nabla} \mathbf{W} + \int_{\partial\Omega} \vec{\mathbf{F}}(\mathbf{U}) \cdot \vec{n} \mathbf{W} - \sum_K \int_K \mathbf{S} \mathbf{W} \\ + \sum_K \int_K D(\mathbf{U}) \vec{\nabla} \mathbf{U} \cdot \vec{\nabla} \mathbf{W} - \int_{\partial\Omega} D(\mathbf{U}) \vec{\nabla} \mathbf{U} \cdot \vec{n} \mathbf{W} = 0 \end{aligned} \quad (34)$$

The integrals over the elements K are evaluated using a numerical quadrature. The MOOSE framework provides a wide range of test functions and quadrature rules. Linear Lagrange polynomials are employed as test functions in the results section. Second-order spatial convergence will be demonstrated for smooth solutions.

5.1.2. Temporal integration

The MOOSE framework offers both first- and second-order explicit and implicit temporal integrators. In all of the numerical examples presented in Section 6, the temporal derivative will be evaluated using the second-order, backward difference temporal integrator BDF2. By considering three consecutive solutions, U^{n-1} , U^n and U^{n+1} , at times t^{n-1} , t^n and t^{n+1} , respectively, BDF2 can be expressed as:

$$\int_K \partial_t \mathbf{U} \mathbf{W} = \int_K (\omega_0 \mathbf{U}^{n+1} + \omega_1 \mathbf{U}^n + \omega_2 \mathbf{U}^{n-1}) \mathbf{W} \quad (35)$$

with

$$\begin{aligned} \omega_0 = \frac{2\Delta t^{n+1} + \Delta t^n}{\Delta t^{n+1} (\Delta t^{n+1} + \Delta t^n)}, \quad \omega_1 = -\frac{\Delta t^{n+1} + \Delta t^n}{\Delta t^{n+1} \Delta t^n} \\ , \text{ and } \omega_2 = \frac{\Delta t^{n+1}}{\Delta t^n (\Delta t^{n+1} + \Delta t^n)} \end{aligned}$$

where $\Delta t^n = t^n - t^{n-1}$ and $\Delta t^{n+1} = t^{n+1} - t^n$.

5.2. Boundary conditions

Boundary conditions are implemented by performing a characteristic decomposition to compute the appropriate flux at the boundaries. Our implementation of the subsonic boundary conditions is inspired of the method described in [21] and was adapted for an temporal implicit solver. Neumann boundary conditions are used for all of the boundary types, except for the inlet supersonic boundary that are imposed with Dirichlet boundary conditions.

For each numerical solution presented in Section 6, the type of boundary conditions used will be specified and taken among the following: supersonic inlet, subsonic inlet (stagnation pressure boundary) and supersonic outlet. The artificial diffusion coefficient $D(\mathbf{U})$ is set to zero at the boundary of the computational domain so that the boundary term $\int_{\partial\Omega} D(\mathbf{U}) \vec{\nabla} \mathbf{U} \cdot \vec{n} \mathbf{W}$ stemming from the integration by parts of the artificial dissipative terms in Eq. (34) is ignored.

5.3. Solver

A Jacobian-free-Newton-Krylov (JFNK) method is used to solve for the solution at the end of each time step. An approximate Jacobian matrix of the discretized equations was derived and implemented. Obtaining the matrix entries requires that the partial derivatives of pressure with respect to the conservative variables be known (this is relatively simple for the Stiffened and Ideal Gas equations of state but may be more complex for general equations of state). The contributions of the artificial dissipative terms to the Jacobian matrix are approximated by lagging the viscosity coefficients (computing them with the previous solution). For instance, this is shown in Eq. (36) for the dissipative terms present in the continuity equation:

$$\frac{\partial}{\partial \mathbf{U}} \left(\kappa \vec{\nabla} \cdot \rho \vec{\nabla} W \right) \simeq \kappa \vec{\nabla} \cdot \frac{\partial \rho}{\partial \mathbf{U}} \vec{\nabla} W, \quad (36)$$

where \mathbf{U} denotes any of the conservative variables (in the above, we have neglected $\frac{\partial \kappa}{\partial \mathbf{U}}$) and W denotes the component of \mathbf{W} associated with the continuity equation.

6. Numerical Results

1-D and 2-D numerical solutions for the Euler equations with viscous regularization using the entropy viscosity method are presented here. Our results validate the chosen definitions for the viscosity coefficients in the low-Mach limit and verify that the new definitions resolve shocks appropriately.

The first set of 1-D simulations consist of liquid water and steam flowing in a converging-diverging nozzle. This test is of interest for multiple reasons: (a) a steady state can be reached (some stabilization methods are known to have difficulties reaching a steady state, [3, 4]), (b) an analytical solution is available and a space-time convergence study can be performed, (c) it can be performed for liquid and gas phases, wherein the gas phase simulation presents a shock while the liquid-phase simulation has a significantly lower Mach number. Next,

421 a 1-D shock tube test (in a straight pipe), taken from the Leblanc test-case suite
 422 [22], is performed. This test is known to be more challenging than Sod shock
 423 tubes and the fluid’s Mach number varies spatially between 0 and 5. A con-
 424 vergence study is also performed to demonstrate convergence of the numerical
 425 solution to the exact solution. A slow moving shock is also investigated [23].
 426 This test helps in assessing the ability of the method to damp the post-shock
 427 low frequency noise (oscillations). Finally, a strong shock for a liquid phase is
 428 also investigated[24].

429 The initial conditions (density in $kg.m^{-3}$, velocity in $m.s^{-1}$, pressure in Pa)
 for the afore mentioned 1-D shock tubes are given in Table 1.

ρ_{left}	u_{left}	P_{left}	ρ_{right}	u_{right}	P_{right}
Leblanc shock tube (Section 6.3)					
1	0	$4 \cdot 10^{-2}$	10^{-3}	0	$4 \cdot 10^{-11}$
Strong shock for liquid phase (Section 6.4)					
1000	0	10^9	1000	0	10^5
Slow moving shock (Section 6.5)					
1	-0.81	1	3.86	-3.44	10.33

Table 1: Initial conditions for the 1-D shock tube tests.

430
 431 2-D simulations are presented next. First, 2-D subsonic flows around a
 432 cylinder [11] and over a Gaussian hump [25] are presented for various far-field
 433 Mach numbers (as low of 10^{-7}). Numerical results of a transonic flow over a
 434 compression corner are provided to illustrate the ability of the new viscosity
 435 definitions to handle supersonic flows. Convergence studies are performed when
 436 analytical solutions are available.

437 For each simulation, data relative to the boundary conditions, the Courant-
 438 Friedrichs-Lewy number (CFL), mesh and equation of state are provided. All
 439 of the numerical solutions presented are obtained using BDF2 as temporal inte-
 440 grator and linear (1-D mesh), \mathbb{P}_1 (2-D triangular mesh), \mathbb{Q}_1 (2-D quadrangular
 441 mesh) finite elements. The spatial integrals are numerically computed using a
 442 second-order Gauss quadrature rule. The steady-state solution is detected from
 443 the transient by monitoring the norm of the total residual (including all of the
 444 equations) and noting when the norm of the total residual falls below 10^{-6} .
 445 The ideal gas [26] or stiffened gas equations of state [27] are used; a generic
 446 expression is given in Eq. (37).

$$P = (\gamma - 1)\rho(e - q) - \gamma P_{\infty} \quad (37)$$

where the parameters γ , q , and P_{∞} are fluid-dependent and are given in Table 2.
 The ideal gas equation of state is recovered by setting $q = P_{\infty} = 0$ in Eq. (37).
 The entropy function for the stiffened gas equation of state is convex and given
 by

$$s = C_v \ln \left(\frac{P + P_{\infty}}{\rho^{\gamma-1}} \right),$$

Table 2: Stiffened Gas Equation of State parameters for steam and liquid water.

fluid	γ	C_v ($J.kg^{-1}.K^{-1}$)	P_∞ (Pa)	q ($J.kg^{-1}$)
liquid water (Section 6.1)	2.35	1816	10^9	$-1167 \cdot 10^3$
steam (Section 6.2)	1.43	1040	0	$2030 \cdot 10^3$
liquid water (Section 6.4)	4.4	1000	$6 \cdot 10^8$	0

where C_v is the heat capacity at constant volume.

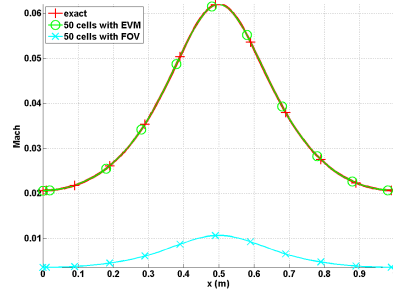
Finally, the convergence rates are computed using the following relation

$$rate_h = \ln \left(\frac{\|U_{2h} - U_{\text{exact}}\| - \|U_h - U_{\text{exact}}\|}{\|U_h - U_{\text{exact}}\|_h - \|U_{h/2} - U_{\text{exact}}\|} \right) / \ln 2 \quad (38)$$

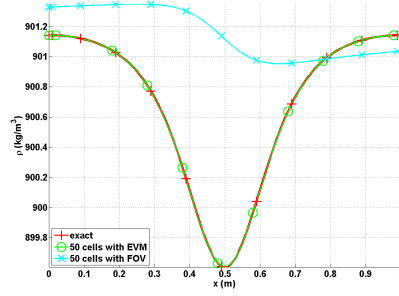
where $\|\cdot\|$ denotes either the L_1 or L_2 norms and h is the characteristic grid size.

6.1. Liquid water in a 1-D converging-diverging nozzle

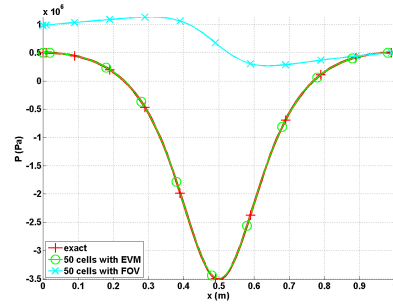
This simulation uses the Euler equations to solve liquid water flowing through a 1-D converging-diverging nozzle of length $L = 1m$ and $A(x) = 1 + 0.5 \cos(2\pi x/L)$. At the inlet, the stagnation pressure and temperature are set to $P_0 = 1MPa$ and $T_0 = 453K$, respectively. At the outlet, only the static pressure is specified: $P_s = 0.5MPa$. Initially, the liquid is at rest, the temperature is uniform and equal to the stagnation temperature and the pressure linearly decreases from the stagnation pressure inlet value to the static pressure outlet value. The stiffened gas equation of state is used to model the liquid water with the parameters provided in Table 2. Because of the low pressure difference between the inlet and the outlet, the smooth initial conditions, and the large value of P_∞ , the flow remains subsonic and thus displays no shock. A detailed derivation of the exact steady-state solution can be found in [28]. A uniform mesh of 50 cells was used to obtain the numerical solution and the time step size was computed using a CFL number of 750. Plots of the Mach number, density, and pressure are given at steady-state in Fig. 1 for the numerical and exact solutions. The viscosity coefficients are also graphed in Fig. 1d.



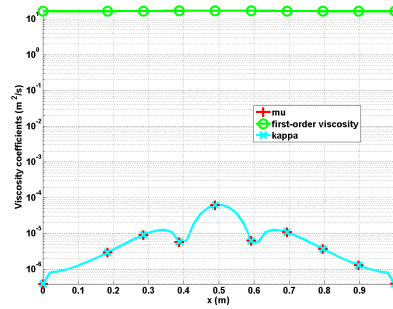
(a) Mach number



(b) Density



(c) Pressure



(d) Viscosity coefficients

Figure 1: Steady-state solution for a liquid flowing through a 1-D converging-diverging nozzle.

469 In Fig. 1, the numerical solutions obtained using the first-order viscosity
 470 (FOV) and the entropy viscosity method (EVM) are plotted against the ex-
 471 act solution. The numerical solution obtained with the EVM and the exact
 472 solution overlap, even for a fairly coarse mesh (50 cells). On the other hand,
 473 the numerical solution obtained with the FOV does not give the correct steady
 474 state: this is an illustration of the effect of ill-scaled dissipative terms. Note
 475 that the entropy viscosity coefficient is very small compared to the first-order
 476 one (Fig. 1d): (i) the numerical solution is smooth as shown in Fig. 1 and (ii)
 477 the flow is in a low-Mach regime and thus isentropic. A convergence study
 478 was performed using the exact solution as a reference: the L_1 and L_2 norms
 479 of the error and the corresponding convergence rates are computed at steady
 480 state on various uniform mesh from 4 to 256 cells. Spatial convergence results
 481 using linear finite elements are reported in Table 3 and Table 4 for the primitive
 482 variables: density, velocity and pressure.

Table 3: L_1 norm of the error for the liquid phase in a 1-D converging-diverging nozzle at steady state.

cells	density	rate	pressure	rate	velocity	rate
4	$2.8037 \cdot 10^{-1}$	—	$8.4705 \cdot 10^5$	—	7.2737	—
8	$1.3343 \cdot 10^{-1}$	0.495	$4.7893 \cdot 10^5$	0.24	6.1493	0.0747
16	$2.9373 \cdot 10^{-2}$	2.10	$1.0613 \cdot 10^5$	2.09	1.2275	2.25
32	$5.1120 \cdot 10^{-3}$	2.58	$1.8446 \cdot 10^4$	2.58	$1.8943 \cdot 10^{-1}$	2.78
64	$1.0558 \cdot 10^{-3}$	2.31	$3.7938 \cdot 10^3$	2.31	$3.7919 \cdot 10^{-2}$	2.37
128	$2.3712 \cdot 10^{-4}$	2.18	$8.4471 \cdot 10^2$	2.19	$8.5517 \cdot 10^{-3}$	2.17
256	$5.6058 \cdot 10^{-5}$	2.08	$1.9839 \cdot 10^2$	2.09	$2.0475 \cdot 10^{-3}$	2.07
512	$1.3278 \cdot 10^{-5}$	2.07	$4.6622 \cdot 10^1$	2.08	$4.9516 \cdot 10^{-4}$	2.06
1024	$3.1193 \cdot 10^{-6}$	—	$1.1755 \cdot 10^1$	—	$1.2379 \cdot 10^{-4}$	—

Table 4: L_2 norm of the error for the liquid phase in a 1-D converging-diverging nozzle at steady state.

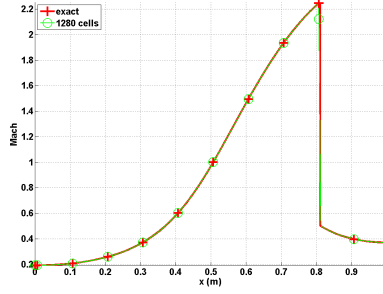
cells	density	rate	pressure	rate	velocity	rate
4	$3.106397 \cdot 10^{-1}$	—	$5.254445 \cdot 10^5$	—	3.288543	—
8	$7.491623 \cdot 10^{-2}$	2.06	$1.636966 \cdot 10^5$	1.62	1.823880	0.14
16	$2.079858 \cdot 10^{-2}$	1.81	$4.627338 \cdot 10^4$	1.77	$4.990605 \cdot 10^{-1}$	1.83
32	$5.329627 \cdot 10^{-3}$	1.96	$1.180287 \cdot 10^4$	1.96	$1.261018 \cdot 10^{-1}$	1.98
64	$1.341583 \cdot 10^{-3}$	1.99	$2.967104 \cdot 10^3$	1.99	$3.160914 \cdot 10^{-2}$	1.99
128	$3.359766 \cdot 10^{-4}$	1.99	$7.428087 \cdot 10^2$	1.99	$7.907499 \cdot 10^{-3}$	1.99
256	$8.403859 \cdot 10^{-5}$	1.99	$1.857861 \cdot 10^2$	2.01	$1.977292 \cdot 10^{-3}$	2.00
512	$2.10075 \cdot 10^{-5}$	—	$4.7024 \cdot 10^1$	—	$4.9516 \cdot 10^{-4}$	—

483 It is observed that the convergence rate for the L_1 and L_2 norm of the error

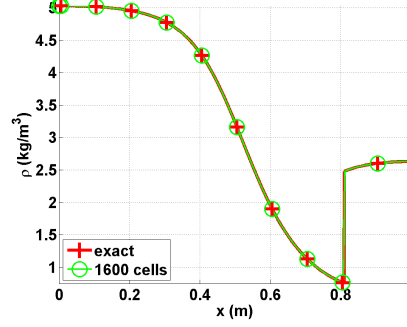
484 is 2; the entropy viscosity method preserves the high-order accuracy when the
485 numerical solution is smooth, and the new definition of the entropy viscosity
486 coefficient behaves appropriately in the low-Mach limit.

487 *6.2. Steam in a 1-D converging-diverging nozzle*

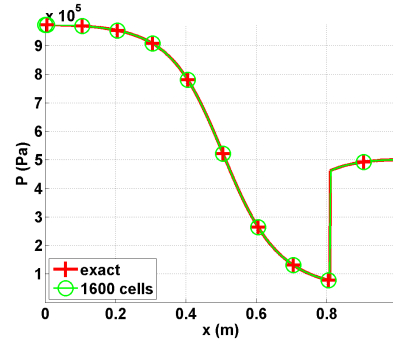
488 We use the same nozzle geometry, initial conditions and boundary conditions
489 as in the previously example but replace liquid water with steam and use the
490 steam parameters of the stiffened gas equation of state, Table 2. In this example,
491 compressible effects will become dominant. The pressure difference between the
492 inlet and outlet is large enough to accelerate the steam through the nozzle,
493 leading to the formation of a shock in the diverging portion of the nozzle. The
494 behavior is different from that observed for the liquid water phase in Section 6.1
495 because of the liquid to gas density ratio is about 1,000. An exact solution at
496 steady state is available for the gas phase [28]. The aim of this section is to show
497 that when using the new definitions of the viscosity coefficients (Eq. (29)), the
498 shock can be correctly resolved without spurious oscillations. The steady-state
499 numerical solution, obtained using a uniform mesh with 1600 cells, is shown in
500 Fig. 2. The CFL was set to 80 (a high CFL value can be used because the
501 shock is stationary).



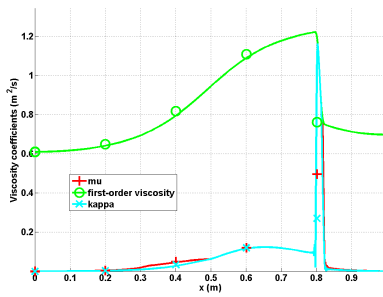
(a) Mach number



(b) Density



(c) Pressure



(d) Viscosity coefficients

20
Figure 2: Steady-state solution for vapor phase flowing in a 1-D converging-diverging nozzle.

502 The steady-state solution of the density, Mach number and pressure are
 503 given in Fig. 2. The steady-solution exhibits a shock around $x = 0.8m$ and
 504 matches the exact solution. In Fig. 2d, the first-order and entropy viscosity
 505 coefficients are plotted at steady-state (on a log scale): the entropy viscosity
 506 coefficient is peaked in the shock region around $x = 0.8m$ as expected where it
 507 saturates to the first-order viscosity coefficient. The graph also presents another
 508 peak at $x = 0.5m$ corresponding to the position of the sonic point for a 1-D
 509 converging-diverging nozzle. This particular point is known to exhibit small
 510 instabilities that are detected when computing the jumps of the pressure and
 511 density gradients. Everywhere else, the entropy viscosity coefficient is small.
 512 In order to prove convergence of the numerical solution to the exact solution,
 513 a convergence study is performed. Because of the presence of a shock, second-
 514 order accuracy is not expected and the convergence rate of a numerical solution
 515 should be 1 and $1/2$ when measured in the L_1 and L_2 norms, respectively (see
 516 Theorem 9.3 in [29]). Results are reported in Table 5 and Table 6 for the
 517 primitive variables: density, velocity and pressure. The convergence rates for
 518 the L_1 and L_2 norms of the error computed using Eq. (38) are in good agreement
 with the theoretical values.

Table 5: L_1 norm of the error for the vapor phase in a 1-D converging-diverging nozzle at steady state.

cells	density	rate	pressure	rate	velocity	rate
5	$0.72562 \cdot 10^{-1}$	—	$1.5657 \cdot 10^5$	—	173.69	—
10	$0.4165 \cdot 10^{-1}$	0.80088	$9.6741 \cdot 10^4$	0.63425	120.69	0.52519
20	$0.20675 \cdot 10^{-1}$	1.0104	$4.9193 \cdot 10^4$	0.96971	72.149	0.74228
40	$0.093703 \cdot 10^{-1}$	1.1417	$2.0103 \cdot 10^4$	0.72728	34.716	1.0554
80	$0.047328 \cdot 10^{-1}$	0.9854	$1.0208 \cdot 10^4$	0.9777	16.082	1.1101
160	$0.023965 \cdot 10^{-2}$	0.9817	$5.1969 \cdot 10^3$	0.9739	7.9573	1.0150
320	$0.020768 \cdot 10^{-2}$	0.9886	$2.5116 \cdot 10^3$	1.0490	3.7812	1.0734
640	$0.0059715 \cdot 10^{-2}$	1.0160	$1.2754 \cdot 10^3$	0.9776	1.8353	1.0428

519

Table 6: L_2 norm of the error for the vapor phase in a 1-D converging-diverging nozzle at steady state.

cells	density	rate	pressure	rate	velocity	rate
5	$9.7144 \cdot 10^{-1}$	—	$2.0215 \cdot 10^5$	—	236.94	—
10	$5.9718 \cdot 10^{-1}$	0.70195	$1.3024 \cdot 10^5$	0.63425	166.56	0.50854
20	$2.9503 \cdot 10^{-1}$	1.0173	$6.6503 \cdot 10^4$	0.96971	103.36	0.68831
40	$1.8193 \cdot 10^{-1}$	0.69747	$4.0171 \cdot 10^4$	0.72728	66.374	0.6390
80	$1.3366 \cdot 10^{-1}$	0.44485	$2.3163 \cdot 10^4$	0.43576	42.981	0.62692
160	$9.6638 \cdot 10^{-2}$	0.46790	$1.7263 \cdot 10^4$	0.42413	31.717	0.43844
320	$7.0896 \cdot 10^{-2}$	0.44688	$1.2763 \cdot 10^4$	0.43571	23.138	0.45499
640	$5.2191 \cdot 10^{-2}$	0.44190	$9.4217 \cdot 10^3$	0.43790	16.910	0.45238

6.3. Leblanc shock tube

The 1-D Leblanc shock tube is a Riemann problem designed to test the robustness and the accuracy of stabilization methods. The initial conditions are given in Table 1. The ideal gas equation of state (with $\gamma = 5/3$) is used to compute the pressure. This test is computationally challenging because of the large pressure ratio at the initial interface. The computational domain consists of a 1-D straight pipe of length $L = 9m$ with the initial interface located at $x = 2m$. At $t = 0.s$, the interface is removed. The numerical solution is run until $t = 4s$ and the density, momentum and total energy profiles are given in Fig. 3, along with the exact solution. The viscosity coefficients are also plotted in Fig. 3d. These plots were run with three different uniform meshes of 800, 3200 and 6000 cells and a constant $CFL = 1$.

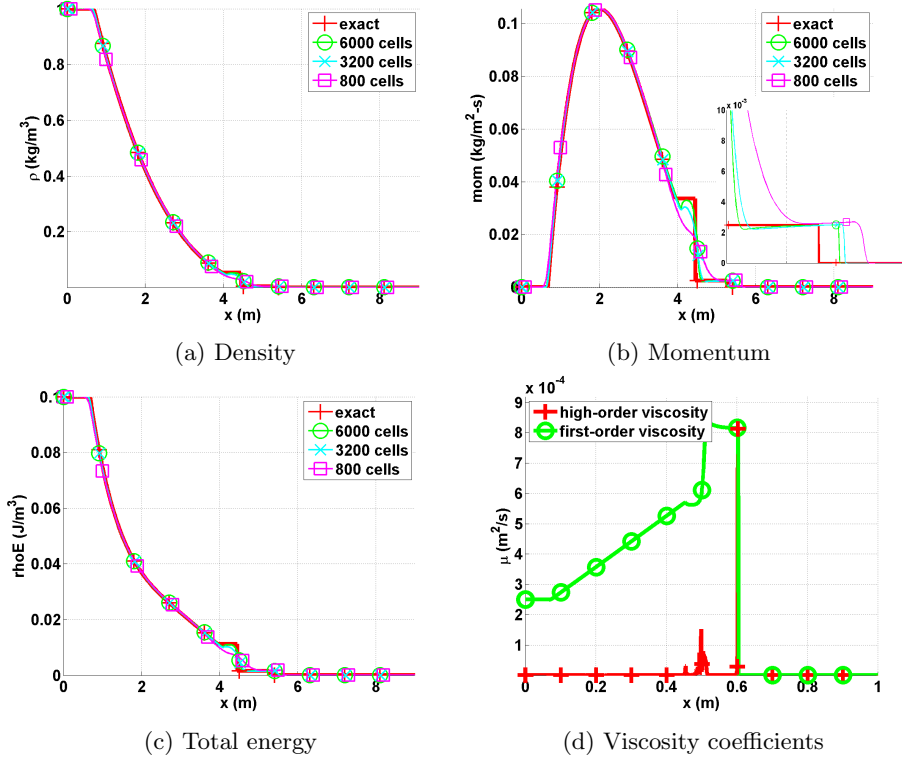


Figure 3: Exact and Numerical solutions for the 1-D Leblanc shock tube at $t = 4s$.

The density, momentum and total energy profiles are provided in Fig. 3. In Fig. 3b, the shock region is zoomed in for better resolution: the shock is well resolved. We also observe that the shock position computed numerically converges to the exact position under mesh refinement. The contact wave at $x = 4.5m$ can be seen in Fig. 3b. The entropy viscosity coefficient profile is shown in Fig. 3d and behaves as expected: it saturates to the first-order viscosity in the shock region, thus preventing oscillations from forming. At the location of the contact wave, a smaller peak is observed that is due to the presence of the jumps in the definition of the entropy viscosity coefficient (Eq. (29)). The Mach number, not plotted, is of the order of 1.3 just before the shock and reaches a maximum value close to 5 in the contact region.

Once again, a convergence study is performed in order to prove convergence of the numerical solution to the exact solution. As in the previous example (vapor phase in the 1-D nozzle, Section 6.2), the expected convergence rates in the L_1 and L_2 norms are 1 and $1/2$, respectively. The exact solution was obtained by running a 1-D Riemann solver and used as the reference solution to compute the L_1 and L_2 -norms that are reported in Table 7 and Table 8 for the

conservative variables: density, momentum and total energy. The convergence rates are again approaching the theoretical values.

Table 7: L_1 norm of the error for the 1-D Leblanc test at $t = 4s$.

cells	density	rate	momentum	rate	total energy	rate
100	$1.0354722 \cdot 10^{-2}$	—	$3.5471714 \cdot 10^{-3}$	—	$1.4033046 \cdot 10^{-3}$	—
200	$7.2680512 \cdot 10^{-3}$	0.51064841	$2.5933119 \cdot 10^{-3}$	0.45187331	$9.8611746 \cdot 10^{-4}$	0.5089968
400	$5.0825628 \cdot 10^{-3}$	0.51601245	$2.0668092 \cdot 10^{-3}$	0.32739054	$7.7844421 \cdot 10^{-4}$	0.34116585
800	$3.4025056 \cdot 10^{-3}$	0.57895861	$1.4793838 \cdot 10^{-3}$	0.48240884	$5.5702549 \cdot 10^{-4}$	0.48285029
1600	$2.1649953 \cdot 10^{-3}$	0.65223363	$9.7152832 \cdot 10^{-4}$	0.6066684	$3.5720171 \cdot 10^{-4}$	0.64100438
3200	$1.2465433 \cdot 10^{-3}$	0.79643094	$5.5937409 \cdot 10^{-4}$	0.79644263	$2.0491799 \cdot 10^{-4}$	0.80169235
6400	$6.4476928 \cdot 10^{-4}$	0.95107804	$3.0244198 \cdot 10^{-4}$	0.88715502	$1.0914891 \cdot 10^{-4}$	0.90874889
12800	$3.3950948 \cdot 10^{-4}$	0.92533116	$1.5958118 \cdot 10^{-4}$	0.9223679	$5.7909794 \cdot 10^{-5}$	0.91441847

Table 8: L_2 norm of the error for the 1-D Leblanc test at $t = 4s$.

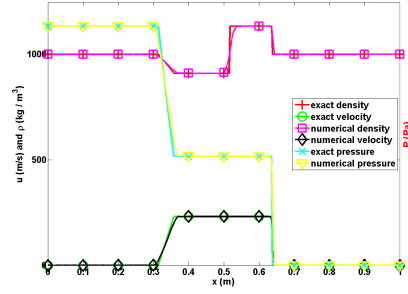
cells	density	rate	momentum	rate	total energy	rate
100	$5.7187851 \cdot 10^{-3}$	—	$1.7767236 \cdot 10^{-3}$	—	$7.6112265 \cdot 10^{-4}$	—
200	$3.8995238 \cdot 10^{-3}$	0.55241073	$1.4913161 \cdot 10^{-3}$	0.25263314	$5.5497308 \cdot 10^{-4}$	0.45571115
400	$2.8103526 \cdot 10^{-3}$	0.4725468	$1.3305301 \cdot 10^{-3}$	0.164585	$4.6063172 \cdot 10^{-4}$	0.26880405
800	$2.1081933 \cdot 10^{-3}$	0.41474398	$1.1398931 \cdot 10^{-3}$	0.22310254	$3.7798953 \cdot 10^{-4}$	0.28526749
1600	$1.5731052 \cdot 10^{-3}$	0.42239201	$9.0394227 \cdot 10^{-4}$	0.33459602	$2.9584646 \cdot 10^{-4}$	0.35349763
3200	$1.0610667 \cdot 10^{-3}$	0.56809979	$6.2735595 \cdot 10^{-4}$	0.52694639	$2.054455 \cdot 10^{-4}$	0.52609289
6400	$7.3309974 \cdot 10^{-4}$	0.53343397	$4.4545754 \cdot 10^{-4}$	0.49399631	$1.4670834 \cdot 10^{-4}$	0.48580482
12800	$5.1020991 \cdot 10^{-4}$	0.52291857	$3.1266758 \cdot 10^{-4}$	0.5106583	$1.0299897 \cdot 10^{-5}$	0.51032105

6.4. 1-D shock tube with a liquid phase

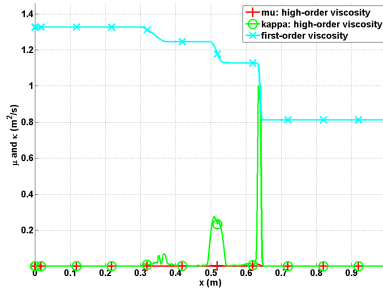
The purpose of this test is to investigate the ability of the entropy viscosity method to stabilize a strong shock with a small Mach number [24] (this reference is for a two-phase flow model but we are only interested in the initial conditions for the liquid phase): the Mach number in the shock region is of the order of 0.1. In this case, as explained in Section 3.2, the viscosity coefficients are required to have different order of magnitude in order to ensure the correct scaling of the dissipative terms. The purpose of this test is to validate the approach presented in Section 3.2.

The stiffened gas equation of state is used to model a liquid flow with the parameters given in Table 2. The computational domain of length $L = 1m$ is uniformly discretized using 500 cells. The step initial conditions are given in Table 1. The simulation is run with a $CFL = 1$ until the final time $t_{\text{final}} = 7 \cdot 10^{-5}s$. Results for pressure, density, velocity and the viscosity coefficients

are given in Fig. 4 along with the exact solution for comparison purposes. The numerical solution is in good agreement with exact solution in Fig. 4a. The viscosity coefficients μ and κ are not equal in the shock because the Mach number is of order 0.1. The viscosity coefficient κ saturates to the first-order viscosity in the shock region around $x = 0.65m$ and is sufficient to stabilize the numerical scheme.



(a) Density, velocity and pressure profiles.



(b) Viscosity coefficients profile.

Figure 4: Numerical solution for the 1-D liquid shock tube at $t_{\text{final}} = 7 \cdot 10^{-5} s$.

6.5. 1-D slow moving shock

Slow moving shocks are known to produce post-shock noise of low frequency that is not damped by some numerical dissipation methods [23]. The aim of this simulation is to test the ability of the entropy viscosity method to dampen the low frequency waves. The 1-D slow moving shock consists of a shock wave moving from left to right with the initial conditions given in Table 1. The ideal gas equation of state is used with a heat capacity ratio $\gamma = 1.4$. In order to make the shock travel a significant distance, the final time is taken equal to $t = 1.1s$. A pressure boundary condition is used at the left boundary to let the rarefaction and contact waves exit the domain. The numerical solution, obtained with 200 equally-spaced cells, is given in Fig. 5 and is compared to the exact solution obtained from a Riemann solver. We use a CFL of 1. With this CFL value, it takes about 50 time steps for the shock to traverse one cell. The numerical

584 results are in good agreement with the exact solution and do not display any
 585 post-shock noise. The rarefaction and contact waves are not visible on Fig. 5a
 586 since they exited the computational domain through the left pressure boundary
 587 condition earlier. As explained in [30], Godunov's type method usually fails to
 588 resolve a slow moving shock because of the nature of the stabilization method:
 589 the method scales as the eigenvalue of the appropriate field. In the case of a slow
 590 moving shock, the dissipation added to the system is under-estimated and leads
 591 to post-shock noise. In the case of the entropy viscosity method, the entropy
 592 residual detects the shock position and the viscosity coefficients saturate to the
 593 first-order viscosity values in the shock region. The main difference between a
 594 Godunov's type method and the entropy viscosity method lies in the definition of
 595 the first-order viscosity coefficients that are proportional to the *local maximum*
 596 *eigenvalue* $||\vec{u}|| + c$ and not to the eigenvalue of the characteristic field.

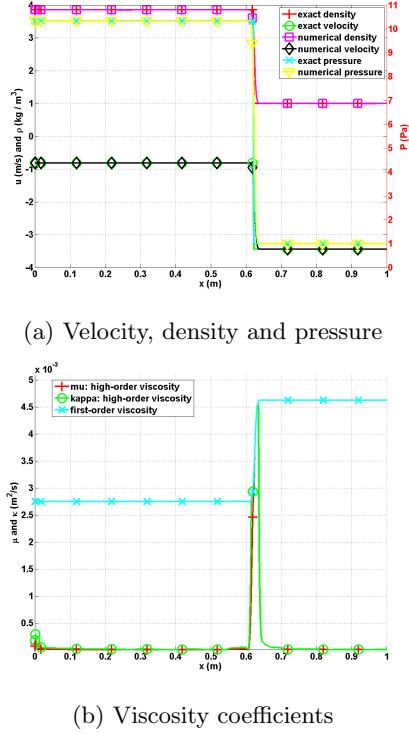


Figure 5: Slow moving shock profiles at $t = 1.1s$.

597 6.6. Subsonic flow over a 2-D cylinder

598 Fluid flow over a 2-D cylinder is often used as a benchmark case to test
 599 numerical schemes in the low-Mach regime [9, 10, 11]. For this test, an analytical
 600 solution is available in the incompressible limit or low-Mach limit and is often

referred to as the potential flow solution. The main features of the potential flow are the following:

- The solution is symmetric: the iso-Mach contour lines are used to assess the symmetry of the numerical solution;
- The velocity at the top of the cylinder is twice the incoming velocity set at the inlet;
- The pressure fluctuations are proportional to the square of inlet Mach number, i.e.,

$$\delta P = \frac{\max(P(\vec{r})) - \min(P(\vec{r}))}{\max(P(\vec{r}))} \propto M_\infty^2 \quad (39)$$

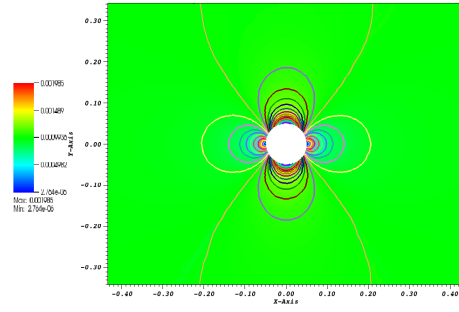
where δP and M_∞ denote the pressure fluctuations and the inlet Mach number, respectively.

The computational domain consists of a 1×1 square with a circular hole of radius 0.05 in its center. A \mathbb{P}_1 triangular mesh with 4008 triangular elements is employed to discretize the geometry. The ideal gas equation of state, with $\gamma = 1.4$ is used. At the inlet, a subsonic stagnation boundary condition is used: the stagnation pressure and temperature are computed using the following relations:

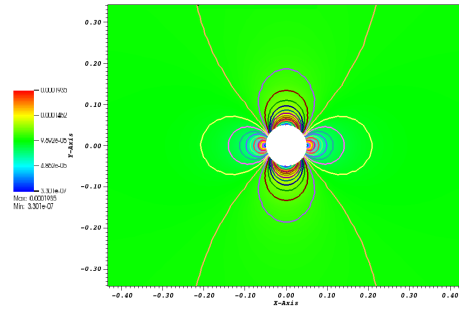
$$\begin{cases} P_0 = P \left(1 + \frac{\gamma-1}{2} M^2\right)^{\frac{\gamma}{\gamma-1}} \\ T_0 = T \left(1 + \frac{\gamma-1}{2} M^2\right) \end{cases} \quad (40)$$

A static pressure boundary condition, with static pressure $P_s = 101,325 \text{ Pa}$, is set for the outlet boundary. The implementation of the pressure boundary conditions is based on [21]. A solid wall boundary condition is set for the top and bottom walls of the computational domain. The simulations are run until a steady state is reached (with a CFL of 40). When the residual norm (for all equations) is less than 10^{-12} the steady state is considered to have been reached.

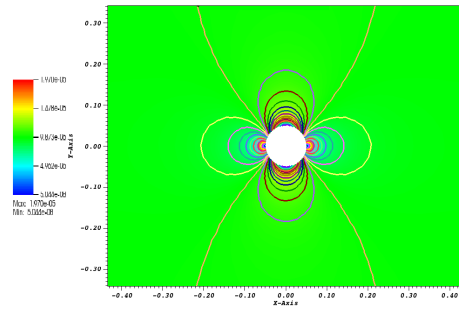
Several simulations are performed, with inlet Mach numbers M_{inlet} ranging from 10^{-3} to 10^{-7} , and are shown in Fig. 6. The iso-Mach contour lines are drawn using 30 equally-spaced intervals $2 \cdot 10^{-10}$ to M_{inlet} which allows the assessment of the symmetry of the numerical solution.



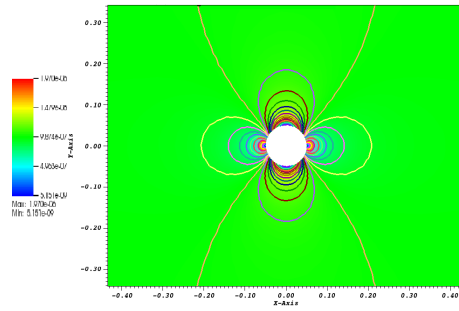
(a) $M_{\text{inlet}} = 10^{-3}$



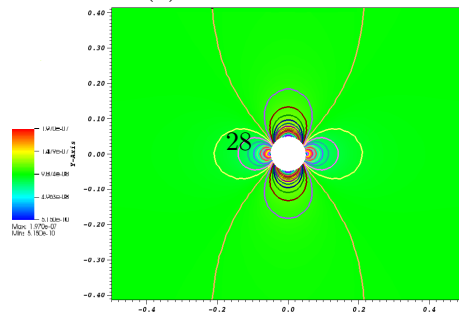
(b) $M_{\text{inlet}} = 10^{-4}$



(c) $M_{\text{inlet}} = 10^{-5}$



(d) $M_{\text{inlet}} = 10^{-6}$



(e) $M_{\text{inlet}} = 10^{-7}$

627 The velocity at the top of the cylinder and at the inlet are given for different
628 Mach-number values (ranging from 10^{-3} to 10^{-7}) in Table 9. The ratio of the
629 inlet velocity to the velocity at the top of cylinder is also computed and is very
630 close to the theoretical value of 2 that is expected in the incompressible limit.

Table 9: Velocity ratio for different Mach numbers.

Mach number	inlet velocity	velocity at the top of the cylinder	ratio
10^{-3}	$2.348 \cdot 10^{-3}$	$1.176 \cdot 10^{-3}$	1.99
10^{-4}	$2.285 \cdot 10^{-4}$	$1.145 \cdot 10^{-4}$	1.99
10^{-5}	$2.283 \cdot 10^{-5}$	$1.144 \cdot 10^{-5}$	1.99
10^{-6}	$2.283 \cdot 10^{-6}$	$1.144 \cdot 10^{-6}$	1.99
10^{-7}	$2.283 \cdot 10^{-7}$	$1.144 \cdot 10^{-7}$	1.99

631 In Fig. 7, the fluctuations in pressure and velocity are plotted as a function
632 of the Mach number (on a log-log scale). The fluctuations are expected to be
633 of the order of M^2 and M for the pressure and velocity, respectively. It is
634 known that some stabilization methods, e.g., [9, 10, 11], can produce pressure
635 fluctuations with the wrong Mach-number order. Here, the entropy viscosity
636 method yields the correct order in the low-Mach limit. For ease of comparison,
637 the reference lines with slope values of 1 and 2 are also plotted.

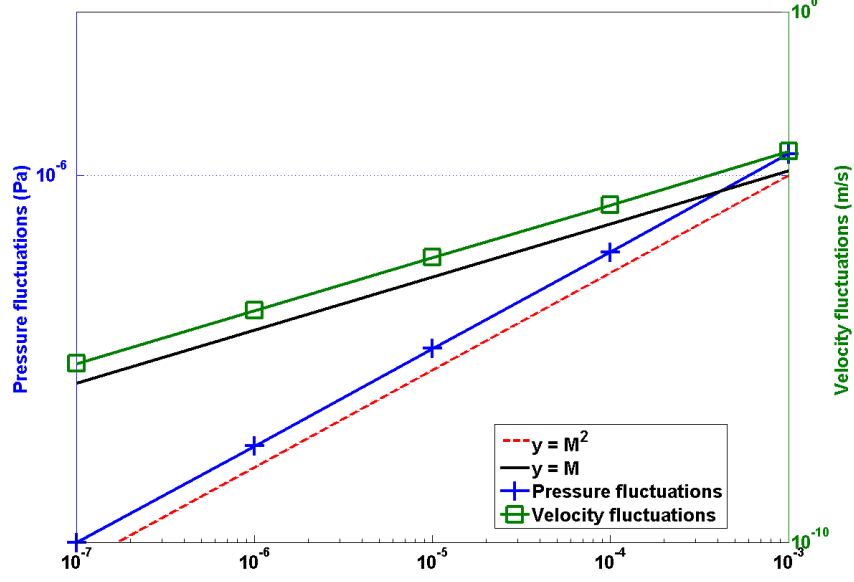


Figure 7: Log-log plot of the pressure and velocity fluctuations as a function of the far-field Mach number.

6.7. Subsonic flow over a 2-D hump

This is another example of an internal flow configuration. It consists of a channel of height $L = 1\text{ m}$ and length $3L$, with a circular bump of length L and thickness $0.1L$. The bump is located on the bottom wall at a distance L from the inlet. The system is initialized with a uniform pressure $P = 101,325\text{ Pa}$ and temperature $T = 300\text{ K}$. The initial velocity is computed from the inlet Mach number, the pressure, the temperature and the ideal gas equation (with $\gamma = 1.4$). Here, $C_v = 717\text{ J/kg} \cdot \text{K}$. At the inlet, a subsonic stagnation boundary condition is used and the stagnation pressure and temperature are computed using Eq. (40). The static pressure $P_s = 101,325\text{ Pa}$ is set at the subsonic outlet. The results are shown in Fig. 8a, Fig. 8b, Fig. 8c and Fig. 8d for the inlet Mach numbers $M_\infty = 0.7$, $M_\infty = 0.01$, $M_\infty = 10^{-4}$ and $M_\infty = 10^{-7}$, respectively. It is expected that, within the low Mach number range, the solution does not depend on the Mach number and is identical to the solution obtained with an incompressible flow code. On the other hand, for a flow at $M = 0.7$, the compressible effects become more important and shock can form. A uniform grid of 3352 Q_1 elements was used to obtain the numerical solution for Mach numbers below $M_\infty = 0.01$. A once-refined mesh was employed for the $M_\infty = 0.7$ simulation in order to better resolve the shock. A CFL of 20 was employed and the simulations were run until steady state.

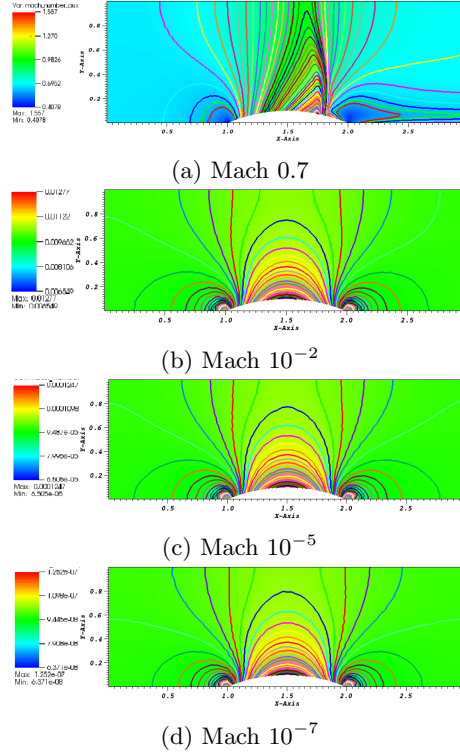


Figure 8: Iso-Mach lines for a 2-D flow over a circular bump (steady-state solution).

The results shown in Fig. 8b, Fig. 8c and Fig. 8d correspond to the low-Mach regime. The iso-Mach lines are drawn ranging from the minimum and the maximum values (provided in each legend) using 50 equally-spaced intervals. The steady-state solution is symmetric and does not depend on the value of the inlet Mach number, as expected in the incompressible limit.

In Fig. 8a, the steady-state numerical solution develops a shock: the compressibility effect are no longer negligible. The iso-Mach lines are also plotted with 50 intervals and range from 0.4 to 1.6. The shock is well resolved and does not display any instabilities or spurious oscillations. The results presented in Fig. 8 were obtained with the new definitions of the viscosity coefficients and illustrate the ability of the entropy viscosity method to correctly simulate several types of flows (subsonic and transonic flows) without tuning parameters.

6.8. Supersonic flow in a compression corner

In this last example, we consider a supersonic flow at Mach 2.5 impinging on a corner with an angle of 15° . From oblique shock theory [15], an analytical solution for this supersonic flow is available which gives the downstream to

upstream pressure, entropy and Mach number ratios. The initial conditions are chosen to be spatially uniform: the pressure and temperature are set to $P = 101,325 \text{ Pa}$ and $T = 300 \text{ K}$, respectively. The ideal gas equation of state is used with the same parameters as in Section 6.7. The initial velocity is computed from the upstream Mach number. The inlet is supersonic and therefore, the pressure, temperature and velocity are specified using Dirichlet boundary conditions. The outlet is also supersonic and none of the characteristics enter the domain through this boundary; the values are computed by the implicit solver.

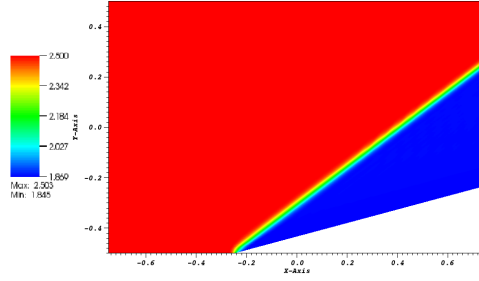
The simulation is run with $CFL = 2$, until steady state is reached. A 2-D mesh made of 16,109 Q_1 elements is used. The ratios for pressure, entropy and Mach number computed using the analytical (published with only two significant digits) and the numerical solutions are given in Table 10; they are in excellent agreement. The shock wave angle at steady state is also known and given by the so-called $\theta - \beta - M$ relation:

$$\tan \theta = 2 \cot \beta \frac{M^2 \sin^2 \beta - 1}{M^2 (\gamma + \cos^2(2\beta)) + 2}, \quad (41)$$

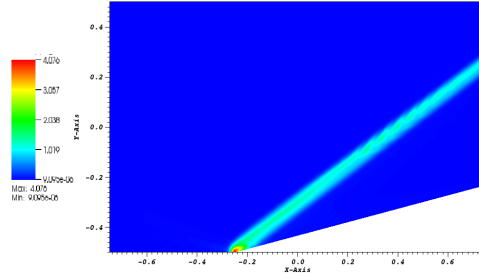
where θ , β and M denote the corner angle, the shock wave angle, and the upstream Mach number, respectively. For Mach 2.5 and a 15° corner angle, the analytical value for the shock wave angle is 36.94° at steady state. From Fig. 9a, the numerical value of the shock wave angle can be measured and is found to be equal to 36.9° , and thus in excellent agreement with theory.

	analytical	numerical
Pressure	2.47	2.467
Mach number	0.74	0.741
Entropy	1.03	1.026

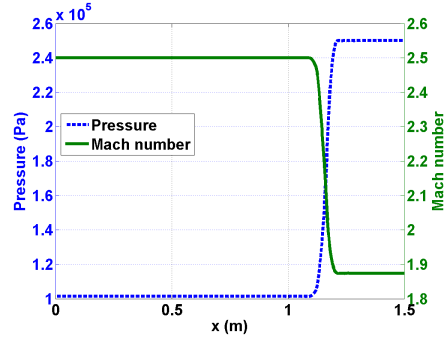
Table 10: Ratio of analytical and numerical downstream to upstream quantities for the compression corner problems (corner angle of 15° and inlet $M = 2.5$ (analytical values from [15])).



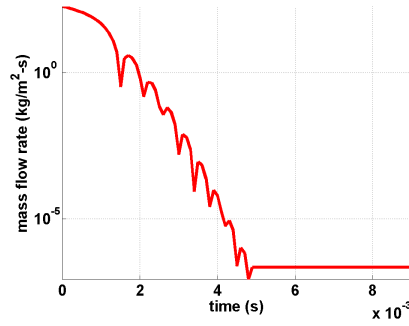
(a) Mach number



(b) Viscosity coefficients



(c) Pressure and Mach number



(d) Difference between inlet and outlet mass flow rates as a function of time.

Figure 9: Steady-state solution for a flow in a 2-D compression corner.

694 The steady-state numerical solution is given in Fig. 9; the Mach number and
 695 the viscosity coefficients are plotted in Fig. 9a and Fig. 9b, respectively. The
 696 steady-state solution is composed of two regions of constant state separated by
 697 an oblique shock. Fig. 9b shows that the viscosity coefficient is large in the shock
 698 and small elsewhere, as expected. At the location of the corner ($x = -0.25m$,
 699 $y = -0.5m$), the viscosity coefficient is peaked because of the treatment of the
 700 wall boundary condition: at this particular node, the normal is not well defined
 701 and may cause some numerical errors. The 1-D graphs at $y = 0$ for the pressure
 702 and the Mach number are given in Fig. 9c: no spurious oscillations are observed
 703 and the shock is well resolved. Finally, the difference between the inlet and
 704 outlet mass flow rates is plotted in Fig. 9d which shows that a steady state has
 705 been reached.

706 7. Conclusions

707 A new version of the entropy viscosity method valid for a wide range of
 708 Mach numbers and applied to the multi-D Euler equations with variable area
 709 was derived and presented. The definition of the viscosity coefficient is now
 710 consistent with the low Mach asymptotic limit, does not require an analytical
 711 expression of gas equations of state. In 1-D, convergence of the numerical so-
 712 lution (either smooth or with shocks) to the exact solution was demonstrated
 713 by computing the convergence rates of the L1 and L2 norms of the error for
 714 flows in a converging-diverging nozzle and a straight pipe. 2-D simulations were
 715 also performed for both subsonic and supersonic flows, and various geometries
 716 wherein the entropy viscosity method behaved well for a wide range of Mach
 717 numbers. The numerical results obtained for a flow over a circular bump (sub-
 718 sonic and transonic flows) illustrated the capabilities of the method to adapt to
 719 the flow type.

720 In the future, the entropy viscosity method will be extended to the seven equa-
 721 tion two-phase model [21]. This two-phase flow system of equations is a good
 722 candidate for two reasons: it is unconditionally hyperbolic and degenerates to
 723 the multi-D Euler equations when one phase disappears.

724 Acknowledgments

725 The authors (M.D. and J.R.) would like to thank Bojan Popov and Jean-Luc
 726 Guermond for many fruitful discussions.

727 References

- 728 [1] J. L. Guermond, R. Pasquetti, Entropy viscosity method for nonlinear con-
 729 servation laws, *Journal of Comput. Phys* 230 (2011) 4248–4267.
- 730 [2] J. L. Guermond, R. Pasquetti, Entropy viscosity method for high-order ap-
 731 proximations of conservation laws, *Lecture Notes in Computational Science*
 732 *and Engineering* 76 (2011) 411–418.

- 733 [3] B. Cockburn, C. Johnson, C. Shu, E. Tadmor, Advanced numerical approx-
734 imation of nonlinear hyperbolic equations, Lecture Notes in Mathematics
735 1697.
- 736 [4] B. Cockburn, G. Karniadakis, C. Shu, Discontinuous galerkin methods:
737 theory, computation and applications, Lecture Notes in Computer Science
738 and Engineering 11.
- 739 [5] R. Lohner, Applied CFD Techniques: an Introduction based on Finite
740 Element Methods, 2nd Edition Wiley, 2003.
- 741 [6] A. Lapidus, A detached shock calculation by second order finite differences,
742 J. Comput. Phys. 2 (1967) 154–177.
- 743 [7] R. Lohner, K. Morgan, J. Peraire, A simple extension to multidimensional
744 problems of the artificial viscosity due to lapidus, Commun. Numer. Meth-
745 ods Eng. 1(14) (1985) 141–147.
- 746 [8] J. Donea, A. Huerta, Finite Element Methods for Flow Problems, Oxford
747 University Press, 2003.
- 748 [9] H. Guillard, C. Viozat, On the behavior of upwind schemes in the low mach
749 number limit, Computers & Fluids 28 (1999) 63–86.
- 750 [10] E. Turkel, Preconditioned techniques in computational fluid dynamics,
751 Annu. Rev. Fluid Mech. 31 (1999) 385–416.
- 752 [11] J. S. W. D. L. Darmofal, J. Peraire, The solution of the compressible euler
753 equations at low mach numbers using a stabilized finite element algorithm,
754 Comput. Methods Appl. Mech. Engrg. 190 (2001) 5719–5737.
- 755 [12] X.-S. Li, C.-W. Gu, An all-speed roe-type scheme and its asymptotic anal-
756 ysis of low mach number behavior, Journal of Computational Physics 227
757 (2008) 5144–5159.
- 758 [13] D. Gaston, C. Newsman, G. Hansen, D. Lebrun-Grandie, A parallel compu-
759 tational framework for coupled systems of nonlinear equations, Nucl. Eng.
760 Design 239 (2009) 1768–1778.
- 761 [14] J. L. Guermond, B. Popov, Viscous regularization of the euler equations
762 and entropy principles, under review.
- 763 [15] J. D. Anderson, Modern compressible flow, in: Guide for Verification and
764 Validation in Computational Solid Mechanic., New York, 1982, pp. 10–
765 2006.
- 766 [16] J. L. Guermond, R. Pasquetti, Entropy-based nonlinear viscosity for four-
767 rier approximations of conservation laws, in: C.R. Math. Acad. Sci., Vol.
768 326, Paris, 2008, pp. 801–806.

- 769 [17] V. Zingan, J. L. Guermond, J. Morel, B. Popov, Implementation of the
770 entropy viscosity method with the discontinuous galerkin method, *Journal*
771 *of Comput. Phys* 253 (2013) 479–490.
- 772 [18] E. F. Toro, *Riemann Solvers and numerical methods for fluid dynamics*,
773 2nd Edition, Springer, 1999.
- 774 [19] B. Muller, Low-mach number asymptotes of the navier-stokes equations,
775 *Journal of Engineering Mathematics* 34 (1998) 97–109.
- 776 [20] T. Alazard, A minicourse on the low mach number limit, *Discrete and*
777 *Continuous Dynamical Systems - Series S* 1 (2008) 365–404.
- 778 [21] R. Berry, R. Saurel, O. LeMetayer, The discrete equation method (dem)
779 for fully compressible, two-phase flows in ducts of spatially varying cross-
780 section, *Nuclear Engineering and Design* 240 (2010) 3797–3818.
- 781 [22] R. Loubere, Validation test case suite for compressible hydrodynamics com-
782 putation, Theoretical Division T-7 Los Alamos National Laboratory.
- 783 [23] J. J. Quirk, A contribution to the great riemann solver debate, NASA
784 Contractor Report 191409 ICASE Report No. (1992) 92–64.
- 785 [24] R. Abgrall, R. Saurel, Discrete equations for physical and numerical
786 compressible multiphase mixtures, *Journal of Computational Physics* 186
787 (2003) 361–396.
- 788 [25] D. L. Darmofal, K. Siu, A robust multigrid algorithm for the euler equations
789 with local preconditioning and semi-coarsening, *Journal of Computational*
790 *Physics* 151 (1999) 728–756.
- 791 [26] P. Perrot, *A to Z of Thermodynamics*, Oxford University Press, 1998.
- 792 [27] O. LeMetayer, J. Massoni, R. Saurel, Elaborating equation of state for a
793 liquid and its vapor for two-phase flow models, *International Journal of*
794 *Thermal Science* 43 (2004) 265–276.
- 795 [28] S. LeMartelot, B. Nkonga, R. Saurel, Liquid and liquid-gas flows at all
796 speeds., *Journal of Computational Physics* 255 (2013) 53–82.
- 797 [29] R. A. DeVore, G. G. Lorentz, *Constructive Approximation*, Springer-
798 Verlag, 1991.
- 799 [30] T. W. Roberts, The behavior of flux difference splitting schemes near slowly
800 moving shock waves, *Journal of Computational Physics* 90 (1990) 141–160.
- 801 [31] L. R. J., *Numerical methods for conservation laws*, Basel: Birhauser, Read-
802 ing, Massachusetts, 1990.

803 **A. Derivation of the entropy residual as a function of density, pres-**
804 **sure and speed of sound**

The entropy residual is defined as follows:

$$R_e(\vec{r}, t) = \partial_t s(\vec{r}, t) + \vec{u} \cdot \vec{\nabla} s(\vec{r}, t),$$

where all variables were defined previously. This form of the entropy residual is not suitable for the low-Mach limit as explained in Section 2.1. In this appendix, we recast the entropy residual $R_e(\vec{r}, t)$ as a function of the primitive variables (pressure, velocity and density) and the speed of sound. The first step of this derivation is to use the chain rule, recalling that the entropy is a function of the internal energy e and the density ρ , yielding

$$R_e(\vec{r}, t) = s_e \frac{De}{Dt} + s_\rho \frac{D\rho}{Dt},$$

805 where s_e denotes the partial derivative of s with respect to the variable e . We
806 recall that $\frac{D}{Dt}$ denotes the material derivative. Since the internal energy e is a
807 function of pressure P and density ρ (through the equation of state), we use
808 again the chain rule to re-express the previous equation as a function of of the
809 material derivatives in P and ρ :

$$\begin{aligned} R_e(\vec{r}, t) &= s_e e_P \frac{DP}{Dt} + (s_e e_\rho + s_\rho) \frac{D\rho}{Dt} \\ &= s_e e_P \left(\frac{DP}{Dt} + \frac{1}{s_e e_P} (s_e e_\rho + s_\rho) \frac{D\rho}{Dt} \right) \\ &= s_e e_P \left(\frac{DP}{Dt} + \left(\frac{e_\rho}{e_P} + \frac{s_\rho}{s_e e_P} \right) \frac{D\rho}{Dt} \right). \end{aligned}$$

To prove that the term multiplying the material derivative of the density is indeed equal to the square of the speed of sound, we recall that the speed of sound is defined as the partial derivative of pressure with respect to density at constant entropy, which can be recast as a function of the entropy as follows (see Appendix A.2 of [14]):

$$c^2 := \left. \frac{\partial P}{\partial \rho} \right|_{s=cst} = P_\rho - \frac{s_\rho}{s_e} P_e.$$

Using the following relations (see Appendix A.1 of [14])

$$P_e = \frac{1}{e_P} \text{ and } P_\rho = -\frac{e_\rho}{e_P},$$

Substitution of these expressions into the entropy residual equation above gives Eq. (9), which is recalled below for completeness:

$$R_e(\vec{r}, t) := \partial_t s + \vec{u} \cdot \vec{\nabla} s = \frac{Ds}{Dt} = \frac{s_e}{P_e} \left(\underbrace{\frac{DP}{Dt} - c^2 \frac{D\rho}{Dt}}_{\widetilde{R}_e(\vec{r}, t)} \right).$$

810 **B. Derivation of the dissipative terms for the Euler equations with**
811 **variable area using the entropy minimum principle**

812 The Euler equations (without viscous regularization) with variable area are
813 recalled here

$$\partial_t (\rho A) + \vec{\nabla} \cdot (\rho \vec{u} A) = 0 \quad (42a)$$

$$\partial_t (\rho \vec{u} A) + \vec{\nabla} \cdot [A (\rho \vec{u} \otimes \vec{u} + P \mathbf{I})] = P \vec{\nabla} A \quad (42b)$$

$$\partial_t (\rho E A) + \vec{\nabla} \cdot [\vec{u} A (\rho E + P)] = 0. \quad (42c)$$

816 The specific entropy is a function of the density ρ and the internal energy e , i.e.,
817 $s(e, \rho)$, the above system of equations satisfies the minimum entropy principle
818 [31].

$$A \rho (\partial_t s + \vec{u} \cdot \vec{\nabla} s) \geq 0. \quad (43)$$

819 The entropy function s satisfies the second law of thermodynamics, $T ds =$
820 $de - \frac{P}{\rho^2} d\rho$, which implies $s_e := T^{-1}$ and $s_\rho := -PT^{-1}\rho^{-2}$. One can show that
821 [14]

$$s_e = T^{-1} \geq 0 \text{ and } P s_e + \rho^2 s_\rho \quad (44)$$

822 In order to apply the entropy viscosity method to the variable-area Euler equa-
823 tions, dissipative terms need to be added to each equation in Eq. (42). The
824 functional forms of these terms need to be such that the entropy residual de-
825 rived with these terms present also satisfies the minimum entropy principle. To
826 prove the minimum entropy principle, the extra terms appearing in the entropy
827 residual are either recast as conservative terms or shown to be positive. The
828 rest of this appendix presents this demonstration. Following [14], we first write
829 the variable-area equation with dissipative terms.

$$\partial_t (\rho A) + \vec{\nabla} \cdot (\rho \vec{u} A) = \vec{\nabla} \cdot f \quad (45a)$$

$$\partial_t (\rho \vec{u} A) + \vec{\nabla} \cdot [A (\rho \vec{u} \otimes \vec{u} + P \mathbf{I})] = P \vec{\nabla} A + \vec{\nabla} \cdot g \quad (45b)$$

$$\partial_t (\rho E A) + \vec{\nabla} \cdot [\vec{u} A (\rho E + P)] = \vec{\nabla} \cdot (h + \vec{u} \cdot g). \quad (45c)$$

where f , g and h are dissipative fluxes to be determined. Starting from the
modified system of equations given in Eq. (45), the entropy residual is derived
again. The derivation requires the following steps : express the governing laws
in terms of primitive variables (ρ, \vec{u}, e) , multiply the continuity equation by ρs_ρ
and the internal energy equation by s_e , and invoke multivariate chain rule, e.g.,
 $\partial s / \partial x = s_e \partial e / \partial x + s_\rho \partial \rho / \partial x$. These steps are similar to those used for the
standard Euler equations [14]. Some of the lengthy algebra is omitted here.
The above steps yield:

$$A \rho (\partial_t s + \vec{u} \cdot \vec{\nabla} s) = s_e \left[\vec{\nabla} \cdot h + g : \vec{\nabla} u + \left(\frac{u^2}{2} - e \right) \vec{\nabla} \cdot f \right] + \rho s_\rho \vec{\nabla} \cdot f \quad (46)$$

832 The next step consists of choosing a definition for each of the dissipative terms
 833 so that the left hand-side is positive. The right hand-side of Eq. (46) can be
 834 simplified using the relations $g = A\mu\vec{\nabla}^s\vec{u} + f \otimes \vec{u}$ and $h = \tilde{h} - 0.5\|\vec{u}\|^2 f$ to give

$$A\rho\left(\partial_t s + \vec{u} \cdot \vec{\nabla} \cdot s\right) = s_e \left[\vec{\nabla} \cdot \tilde{h} - e\vec{\nabla} \cdot f \right] + \rho s_\rho \vec{\nabla} \cdot f + A s_e \mu \vec{\nabla}^s \vec{u} : \vec{\nabla} \vec{u}$$

835 The right hand-side is now integrated by parts:

$$\begin{aligned} A\rho\left(\partial_t s + \vec{u} \cdot \vec{\nabla} \cdot s\right) &= \vec{\nabla} \cdot \left[s_e \tilde{h} - s_e e f + \rho s_\rho f \right] - \\ &\quad \vec{\nabla} \cdot \tilde{h} \vec{\nabla} s_e + f \cdot \vec{\nabla} (e s_e) - f \cdot \vec{\nabla} (\rho s_\rho) + A s_e \mu \vec{\nabla}^s \vec{u} : \vec{\nabla} \vec{u} \end{aligned}$$

836 where $\vec{\nabla}^s$ is the symmetric gradient. The term $A s_e \mu \vec{\nabla}^s \vec{u} : \vec{\nabla} \vec{u}$ is positive and
 837 thus, does not need any further modification. It remains to treat the other
 838 terms of the right hand-side that we now call *rhs*:

$$rhs = \vec{\nabla} \cdot \left[s_e \tilde{h} - s_e e f + \rho s_\rho f \right] - \tilde{h} \cdot \vec{\nabla} s_e + f \cdot \vec{\nabla} (e s_e) - f \cdot \vec{\nabla} (\rho s_\rho)$$

839 The first term of *rhs* is a conservative term. By carefully choosing a definition
 840 for \tilde{h} and f , the conservative term can be expressed as a function of the entropy
 841 s . The inclusion of the variable area in the choice of the dissipative terms is
 842 also required so that, when assuming constant area, the regular multi-D Euler
 843 equations are recovered. The following definitions for \tilde{h} and f are chosen:

$$\tilde{h} = A\kappa\vec{\nabla}(\rho e) \text{ and } f = A\kappa\vec{\nabla}\rho,$$

844 which yields, using the chain rule,

$$rhs = \vec{\nabla} \cdot (\rho A\kappa\vec{\nabla}s) - A\kappa \underbrace{\left[\vec{\nabla}(\rho e) \vec{\nabla} s_e - \vec{\nabla} \rho \vec{\nabla} (e s_e) + \vec{\nabla} \rho \vec{\nabla} (\rho s_\rho) \right]}_{\mathbf{Q}}$$

845 It remains to treat the term \mathbf{Q} that can be recast under a quadratic form.
 846 Following the work done in [14]:

$$\begin{aligned} \mathbf{Q} &= X^t \Sigma X \\ \text{with } X &= \begin{bmatrix} \vec{\nabla} \rho \\ \vec{\nabla} e \end{bmatrix} \text{ and } \Sigma = \begin{bmatrix} \partial_\rho(\rho^2 \partial_\rho s) & \partial_{\rho,e} s \\ \partial_{\rho,e} s & \partial_{e,e} s \end{bmatrix} \end{aligned}$$

847 The matrix Σ is symmetric and identical to the matrix obtained in [14]. The sign
 848 of the quadratic form can be simply determined by studying the positiveness of
 849 the matrix Σ . In this particular case, it is required to prove that the matrix is
 850 negative definite: the quadratic form is in the right hand-side and is preceded
 851 by a negative sign. According to [14], the convexity of negative entropy function
 852 $-s$ with respect to the internal energy e and the specific volume $1/\rho$ is sufficient
 853 to ensure that the matrix Σ is negative definite.

854 Thus, the right hand-side of the entropy residual Eq. (46), are now either recast
 855 as conservative terms, or known to be positive. Following the work done by [14],
 856 the entropy minimum principle holds.

857 **C. Entropy residual with an isentropic equations of state:**

858 This appendix aims to show that the entropy residual is null when assuming
 859 an isentropic flow.

860 The entropy residual as a function of the pressure, density, velocity, and speed
 861 of sound is recalled here:

$$\widetilde{R}_e = \frac{dP}{dt} - c^2 \frac{d\rho}{dt} \quad (47)$$

862 Assuming an isentropic flow, the pressure is only a function of the density $P =$
 863 $f(\rho)$ or $\rho = f^{-1}(P)$. Using the definition of the speed of sound $c^2 = \left. \frac{\partial P}{\partial \rho} \right|_s$ and
 864 the above form of the equation of state, the following relation is derived:

$$c^2 = \left. \frac{\partial P}{\partial \rho} \right|_s = \frac{dP}{d\rho} = \frac{df(\rho)}{d\rho} \quad (48)$$

865 Using the chain rule, the entropy residual of Eq. (47) can be recast as a function
 866 of the density, velocity, and speed of sound, and proven equal to zero:

$$\begin{aligned} \widetilde{R}_e &= \frac{df(\rho)}{d\rho} \frac{d\rho}{dt} - c^2 \frac{d\rho}{dt} \\ \widetilde{R}_e &= c^2 \frac{d\rho}{dt} - c^2 \frac{d\rho}{dt} \\ \widetilde{R}_e &= 0 \end{aligned}$$